学位論文 (博士)

Mechanism of skin barrier function deterioration and development of barrier function-improving agents using *N*-acetylated amino acids

2023 年 3 月

星薬科大学大学院　薬学研究科

大成　宏樹

Contents

List of publications

1. Phase separation in lipid lamellae result from ceramide conformations and lateral packing structure.: H. Ohnari, E. Naru, T. Ogura, O. Sakata, Y. Obata, *Chem. Pharm. Bull.*, 69,72–80 (2021). <presented in Chapter 1 of this dissertation>

2. Distribution of domains formed by lateral packing of intercellular lipid in the stratum corneum.: H. Ohnari, E. Naru, O. Sakata, Y. Obata, *Chem. Pharm. Bull.*, 71, 31–40 (2023). <presented in Chapter 2 of this dissertation>

3. Amino acids and their *n*-acetylated derivatives maintain the skin's barrier function.: H. Ohnari, M. Sekiya, E. Naru, T. Ogura, O. Sakata, Y. Obata, *Chem. Pharm. Bull.*, 69, 652–660 (2021). <presented in Chapter 3 of this dissertation>

Abbreviations

AGLN; *N*-acetyl-L-glutamine

AHYP; *N*-acetyl-L-hydroxyproline, Acetyl hydroxyproline

Ala; L-alanine

Arg; L-(+)-arginine

CER; ceramide

CER[ADS]; *N*-(alpha-hydroxyoctadecanoyl)-dihydrosphingosine

CER[ADS]; alpha-hydroxy-dihydrosphingosine (in chapter 2)

CER[AH]; alpha-hydroxy-6-hydroxysphingosine

CER[AP]; alpha-hydroxy-phytosphingosine

CER[AS]; alpha-hydroxy-sphingosine

CER[NDS]; nonhydroxy-dihydrosphingosine

CER[NP]; nonhydroxy-phytosphingosine

CER[NS]; nonhydroxy-sphingosine

CHOL; cholesterol

DSC; differential scanning calorimetry

ELOVL; fatty acid elongase

ESI-MS/MS; electrospray ionization tandem mass spectrometry

FA; fatty acid

FCO; facecentered orthorhombic

FFA; free fatty acid

FPA; focal plane array

FTIR; fourier transform IR spectroscopy

FWHM; full width at half maximum

Gln; L-glutamine

Glu; glutamic acid

Gly; L-glysine

Hex; hexagonal packing

HEX; hexagonal lateral packing (in chapter 1)

HEX; mainly hexagonal packing domain (in chapter 2)

Hyp; L-hydroxyprolin

LCB; long-chain base

LIQ; mainly liquid crystal domain

NMF; natural moisturizing factors

OR; orthorhombic lateral packing (in chapter 1)

OR; mainly orthorhombic packing domain (in chapter 2)

Orth; orthorhombic packing

PA; palmitic acid

PBS; phosphate-buffered saline

SA; stearic acid

SAXS; small-angle X-ray scattering

SC; stratum corneum

Ser; L-serine

TEWL; transepidermal water loss

WAXD; wide-angle X-ray diffraction

General Introduction

The skin consists of three layers: the epidermis, dermis, and subcutaneous tissue. The outermost epidermis is divided into the stratum corneum (SC), stratum granulosum, stratum spinosum, and stratum basale, in order from the skin's surface. The topmost SC acts as an outside-in skin barrier, preventing the entry of allergens, pathogenic microorganisms, chemicals, and other harmful substances, and as an inside-out skin barrier it inhibits the leakage of water, ions, proteins, and other bodily fluids from the organism.[1)] These skin barrier functions are achieved by the mille-feuille-like multilayered structure of corneocytes and intercellular lipids.

Chemical substances can penetrate the skin through the transcellular, transintercellular, and transappendageal pathways, depending on the substance.[2)] Substances that are easily absorbed transdermally are liposoluble substances with a molecular weight of 500 Da[3)] or less and a log *P* of 1 to 3.[4,5)] The intercellular route is recognized as the primary route of skin penetration.

Intercellular lipids are mainly composed of ceramide (CER), cholesterol (CHOL), and free fatty acids (FFA).[6)] The average molecular weight of these lipids is approximately 500 Da.[7)] These intercellular lipids have a characteristic multilamellar structure, and X-ray scattering measurements show two coexisting lamellar phases with repetition distances of ~13 nm and ~6 nm derived from long- and short-period lamellar structures, respectively.[8)] In addition, the side-aligned packing structures of lipid chains forming this lamellar structure include orthorhombic, hexagonal, and liquid/fluid phases with different packing densities.[9)] When a 500 Da lipophilic molecule is applied to the surface of the SC, it is absorbed into the liquid/fluid phase region by way of the difference in the chemical potential of the interface and it penetrates by diffusion.[7)] The skin barrier function is closely related to the lamellar and packing structures formed by intercellular lipids, and it is extremely important to understand the properties of these structures.

Although it has been suggested that these packing structures have domains,[10)] the details of these domains have not been verified, and the relationship between domain distribution and impaired skin barrier function has not been examined in detail. In addition, several studies have examined the relationship between transepidermal water loss (TEWL), an indicator of skin

barrier function, and packing structure,[11–13] but the participants included patients with inflammatory skin diseases with compromised skin barrier function such as atopic dermatitis, and the relationship between reduced skin barrier function and lipid composition and packing structure in healthy participants has not been fully verified.

To understand the molecular mechanisms of skin barrier formation, the contribution of major lipid classes and subclasses to the lipid composition of intercellular lipids has been studied using lipid model systems. Lipid models range from simple three-component lipid models of the major lipid classes[14–17] to complex compositions of lipid models with more components.[18–20]

Among these, the major lipid class, CER, has a structure in which fatty acids are amide-linked to the amino groups of sphingoid bases, but has structural diversity in the headgroups of its hydrophilic groups. The number of CER subclasses has increased with the evolution of analytical methods,[21–29] and can now be classified into 25 CER subclasses based on differences in the combination of 5 long-chain bases and 5 fatty acids, with 1,327 unbound CERs and 254 protein-bound CERs in 23 subclasses in the human SC.[30]

CERs and FFAs are diversely distributed in chain length[30,31] because the carbon chain lengths of their long-chain bases, fatty acid portions, and fatty acid chains are elongated by the fatty acid elongase ELOVL.[32–36] Therefore, the effects of CER subclasses on packing structure and permeability[37–41] and the chain length of CER subclasses and FFAs have been investigated by using lipid models.[42–45] In skin diseases such as atopic dermatitis[11,28,31] and psoriasis,[46] abnormalities of increased CER[NS] (NS = nonhydroxy-sphingosine) and CER[AS] (AS =alpha-hydroxysphingosine) produced via sphingomyelin and decreased CER[NP] (NP = non-hydroxy-phytosphingosine) and increased short-chain CERs and short-chain FFAs are observed.

On the other hand, there are examples of lipid models that mimic the lipid composition of atopic dermatitis, an inflammatory skin disease, focusing on the sphingosine/sphinganine ratio.[47] However, there are limited examples of the lipid composition of intercellular lipids with impaired skin barrier function in which the effects on lamellar and packing structures were examined in lipid models reflecting not only differences in the CER headgroup structure but

also carbon chain length of CERs and FFAs,[43] and there are no detailed analyses of the properties of packing structures of lamellar structures with different periodicities.

The aim of this study was to elucidate the mechanism of skin barrier function impairment in healthy participants and to identify agents that improve barrier function.

In Chapter 1, I prepared an intercellular lipid model containing alpha-hydroxy CERs and short-chain FFAs with reference to the lipid composition of intercellular lipids with impaired skin barrier function, such as inflammatory skin diseases, to clarify the effects of lipid composition ratio on lamellar structure, packing structure, phase transition, and mixing properties. The purpose of this study was to elucidate the mechanism of skin barrier function degradation. Intercellular lipid models with different lipid composition ratios were prepared and analyzed by differential scanning calorimetry (DSC) and X-ray diffraction measurements.

In Chapter 2, I aimed to clarify the mechanism of skin barrier function degradation in human SC samples with complex lipid compositions by analyzing in detail the differences in CER composition, CER chain length, and packing structure of panel groups with different transdermal water transpiration, an indicator of skin barrier function. The domain distribution of the packing structure was evaluated by Fourier transform infrared spectroscopic imaging. The lipid composition of CER was also validated by measuring it with shotgun lipidomics in electrospray ionization tandem mass spectrometry.

The objective described in Chapter 3 was to screen agents that improve skin barrier function and evaluate whether the selected agents actually have skin barrier function-improving effects. alpha-hydroxy CER-containing intercellular lipid models were prepared, and useful amino acids were screened by DSC. To further confirm the barrier function-improving effect of the selected acetylhydroxyproline, the effect on the lamellar and packing structure of excised human SC was verified by time-resolved small-angle wide-angle X-ray scattering measurements.

CHAPTER 1

Phase separation in lipid lamellae result from ceramide conformations and lateral packing structure

1. Introduction

The SC intercellular lipid not only protects the living body from invasion by allergens and pathogens but also suppresses water evaporation. Thus, it plays a pivotal role in the skin's barrier function.[48] Intercellular lipids are made up of CERs, CHOL, cholesterol esters and FFAs).[29]

Intercellular lipids form a characteristic microstructure, comprising a short lamellar structure and a long lamellar structure with a repeating distance of approximately 6 and 13 nm, respectively.[8] The lamellar period is inversely correlated with TEWL, a representative index of the skin's barrier function.[11,49] In fact, the lamellar period is shorter in patients with atopic dermatitis than in healthy subjects.[11] On the other hand, intercellular lipids of human SC have different packing structures of hydrocarbon chains, and it is known that orthorhombic (Orth) and hexagonal packing (Hex) and liquid crystals coexist as different sublattices.[49] The density of lateral hydrocarbon chain packing is decreased in the order of Orth, Hex, and liquid crystal.[50]

Increasing TEWL indicates deterioration of the SC's barrier function. Some reports have indicated that differences in the hydrocarbon chain packing of intercellular lipids are also correlated with TEWL.[11,12,13] However, it is difficult to elucidate the relationship between lipid composition and packing structure due to the intricate lipid composition of human intercellular lipids; there are 342 CER species, grouped into 12 subclasses on the basis of chain length and head group structure.[24,51] Many studies were conducted to investigate the influence of lipid composition on hydrocarbon chain packing by mimicking the intercellular lipids of the human SC.[17,43,52–59] In this context, some groups reported that two different CER conformations formed in distinct phases of lamellar periodicity.[56–59]

I previously reported that phases of different periodicity coexist in the CER[ADS] (ADS=*N*-(alpha-hydroxyoctadecanoyl)-dihydrosphingosine), CHOL, and palmitic acid (PA) complex model in which structural analysis was carried out using simultaneous small-angle X-ray scattering (SAXS) and wide-angle X-ray diffraction (WAXD) measurements at constant temperature.[17] However, the details of the packing structure of the two phases observed in these intercellular lipid models are unclear. ^{2}H solid-state NMR spectroscopy,[56,57] neutron diffraction measurement, and X-ray diffraction measurement without temperature scanning, could not

discriminate the differences in packing structure in phases with different lamellar periods.[17,56–58)]

In order to determine the characteristics of hydrocarbon chain packing of each lamellar structure, I needed to conduct structural analysis using simultaneous SAXS and WAXD measurements.

The utility of structural analysis of intercellular lipids by simultaneous SAXS and WAXD measurements has previously been reported.[60)] I used intercellular lipid models (CER[ADS]/CHOL/PA) with different lipid compositions from what we have reported previously.[17)] I characterized the packed structure and the lamellar structures by analyzing the temperature-scanning simultaneous SAXS and WAXD measurements against two phases with different lamellar periodicities.

2. Experimental

2.1. Materials

(2*S*,3*R*)-2-(2-hydroxyhexadecanoyl)aminooctadecane-1,3-diol (95%): Ceramide [ADS]-C18/16(CER[ADS]) was supplied by Takasago International (Tokyo, Japan). Cholesterol (CHOL: 99%) and palmitic acid (PA: 99%) were purchased from Sigma-Aldrich (St. Louis, MO). Chloroform and methanol were certified grade. Other chemicals used were reagent grade.

2.2. Lipid model

The lipid composition of the bilayers of CER[ADS], CHOL, and PA selected centroids of three previously reported clusters.[17] The centroids of each cluster (Fig. 1) are representative of the three lipid bilayer groups. In previous reports, clusters were classified into four different types; however, the focus of this study was CER[ADS]. Hence, I selected three models that tended to increase the proportion of CER[ADS] instead. The representative composition of the three models are summarized in Table 1.

The CER[ADS]/CHOL/PA bilayer in Model 1 contains a high molar ratio of PA. In contrast, the CER[ADS]/CHOL/PA bilayer in Model 3 contains a low molar ratio of PA. I observed that the ratio of PA decreases while the ratio of CER and CHOL increases from

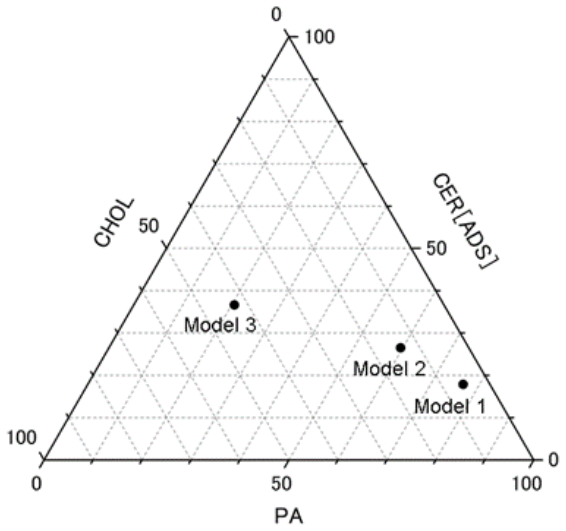

Fig. 1. CER[ADS], CHOL, and PA Models

Closed circles indicate the lipid composition of each model.

Table 1. Composition of Various CER[ADS] Containing Model Lipid Mixtures.

Model	Composition and molar ratio (CER[ADS]/CHOL/PA)	Short lamellar phase A (25 °C)		Short lamellar phase B (25 °C)		Phase separated PA (25 °C)	Phase separated CHOL (25 °C)
		Peak position (nm^{-1})	Repeat distance (nm)	Peak position (nm^{-1})	Repeat distance (nm)		
1	17.8:5.5:76.6	$q1 = 1.362$, $q2 = 2.724$, $q3 = 4.084$	4.61	$q1 = 1.461$, $q2 = 3.019$, $q3 = 4.476$	4.30	+	−
2	26.5:13.9:59.6	$q1 = 1.354$, $q2 = 2.714$, $q3 = 4.048$	4.64	$q1 = 1.447$, $q2 = 2.968$, $q3 = 4.448$	4.34	+	+
3	36.6:42.8:20.6	$q1 = 1.362$, $q2 = 2.724$, $q3 = 4.084$	4.61	$q1 = 1.475$, $q2 = 2.991$, $q3 = 4.462$	4.26	−	+

Lamellar organization with their repeat distances are shown.

Model 1 to Model 3. I prepared our lipid model in accordance with the method of Bangham.[17,61] The lipid mixture is shown in Table 1 was dissolved in chloroform:methanol (2:1, v/v). A rotary evaporator was later used to remove the solvent and obtain a thin lipid film, which was dried in a vacuum for about 24 h. In order to adjust the total lipid concentration to 10 mM in the eggplant flask, 10 mL of acetate buffer (pH 5.3 was added and the lipids hydrated for 30 min above the phase transition temperature (about 85°C). After removing the film from the flask, it was subjected to ultrasonic liquid processor irradiation (VCX 130 PB, Sonics & Materials, Inc., Newtown, CT, U.S.A.) for 5 min above the phase transition temperature (about 85°C). The CER[ADS]/CHOL/PA bilayer suspension was stored at room temperature overnight. The vesicle aggregates were suction-filtered and dried, and used as an intercellular lipid model.

2.3. Simultaneous small-angle X-ray scattering and wide-angle X-ray diffraction measurements

The SAXS and WAXD profiles of the CER[ADS]/CHOL/PA bilayers were obtained at the BL40B2 (Structural Biology II Beamline) in SPring-8 (Hyogo, Japan). The X-ray wavelength was 0.083 nm and the sample-to-detector distance was approximately 540 mm. The scattering intensity I (in arbitrary units) was measured as a function of the scattering angle (θ), from which the scattering vector (q) was calculated in reciprocal nm. The latter is defined as $q = (4\pi \sin \theta)/\lambda$, where λ is the wavelength. From the positions of a series of equidistant peaks (q_n), the periodicity (d) of a lamellar phase was calculated using the equation $d = 2n\pi/q_n$, where n is the order number of the scattering peak. When a characteristic peak position (reciprocal space) is related to the real space, I use the term spacing, which is equal to $2\pi/q$ at that peak

position. The reciprocal spacing $q = (4\pi \sin\theta)/\lambda$ was calibrated from the lattice spacing (d = 5.838 nm; d is the lamellar repeat distance) of a silver behenate crystal at room temperature. The exposure time was 30 s. The diffraction pattern was circular averaged to obtain a radial intensity profile. A sample cell containing the CER[ADS]/CHOL/PA membrane was sealed with a polyimide film and placed in the sample holder of the X-ray diffractometer. The temperature of the sample was controlled between 25°C to 85°C using differential scanning calorimetry (FP-99; Mettler-Toledo, Tokyo, Japan), and the temperature was measured with a thermocouple embedded in the sample holder. All the experiments were performed with a heating scan at a rate of 0.83 K min^{-1}. Hence, the total exposure time was about 72 min in a single scan. The X-ray scattering profile was recorded every 2.5°C.

2.4. Data analysis

I applied Lorentz functions to fit the SAXS profiles and Gaussian functions to fit the WAXD profiles.

In wide-angle analysis, the apparent ratio of hexagonal/orthorhombic hydrocarbon chain packing ($R_{Hex/Orth}$) was defined as:

$$R_{Hex/Orth} = \frac{(I_{15} - 2 \times I_{17}) / 3}{I_{17}}$$

Where I_{15} is the intensity of the diffraction peak at $q \approx 15.0$ nm^{-1}, and I_{17} is that of the peak at $q \approx 17.0$ nm^{-1}. The denominator indicates the apparent area derived from Orth and the numerator indicates the apparent area of Hex. $2 \times I_{17}$ means the apparent area derived from Orth in the area of the diffraction peak at $q \approx 17.0$ nm^{-1}. When Orth and Hex appear in the CER[ADS]/CHOL/PA bilayer at the equivalent ratio, the $R_{Hex/Orth}$ value is 1. Greater $R_{Hex/Orth}$ values indicate that Hex is dominant in the CER[ADS]/CHOL/PA bilayers.

In addition, scattering data were analyzed by generalized indirect Fourier transformation (GIFT) method software package.[62] Using the thickness scattering parameter of a pair distance distribution function (PDDF), $P_t(q)$ corresponds to the convolution of the electron density profile of the mono-bilayer. Hence, electron density profiles i.e. DECON profiles, $\Delta\rho(r)$, can be obtained via deconvolution of the PDDF.[63] The DECON profile is the electron density profile for the lipid bilayer from the hydrophobic group terminal to the

hydrophilic group terminal, including hydration water effects with the electron density of water as the zero ordinate, $\Delta\rho(r) = 0$.

3. Results

3.1.Membrane properties and microstructure of CER[ADS]/CHOL/PA bilayers

I determined the different conformations of our CER[ADS]/CHOL/PA samples. SAXS gives information about ordered multi-lamellar structures and enables detection of lipid lamellar structures and corresponding repeat distances of various lipid membranes. WAXD gives information about the lateral packing present in lamellar structures. When the lipid alkyl chains are packed hexagonally, a singlet is observed at around q = 15 nm^{-1} while lipid tails that partly adopt an Orth result in two peaks at approximately q = 15 and 17 nm^{-1}. The corresponding

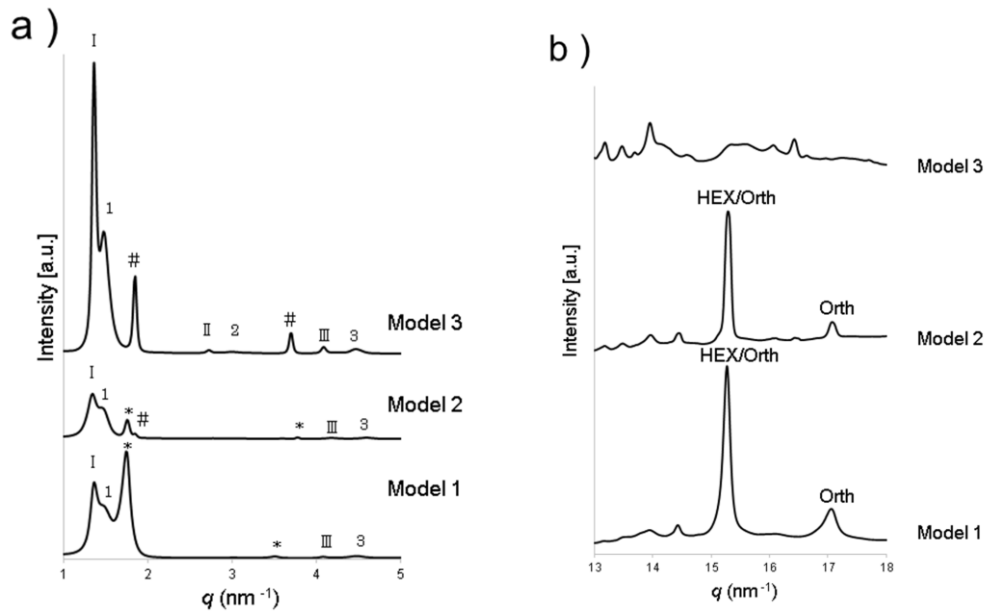

Fig. 2. SAXS and WAXD Profile of Various CER[ADS] Containing Lipid Membranes Used in Our Study

(a) In the SAXS profiles, the Roman numerals (I, II, III…) indicate the different scattering orders of the Phase A, and refer to the orders of scattering peaks of the cell with a repeat distance of 4.6 nm. The Arabic numbers (1, 2, 3…) indicate the different scattering orders of the Phase B, and refer to the orders of scattering peaks of the cell with a repeat distance of 4.3 nm. Peaks originating from the crystalline PA domains are indicated with an asterisk (*). Peaks originating from the crystalline CHOL domains are indicated by the hashtag (#). (b) In the WAXD profiles, Orth and Hex denote reflections attributed to hexagonal, orthorhombic lateral packing, respectively.

scattering patterns of these lipid membranes are shown in Fig. 2.

The scattering patterns of Models 1 and 2 at 25°C (Fig. 2 (a)), are characterized by the presence of scattering peaks at about $q_1 \approx 1.3$, $q_2 \approx 2.7$, and $q_3 \approx 4.1$ nm^{-1}, with a repeat distance of about 4.6 nm. This pattern indicates the formation of the short periodicity phase (Phase A). However, besides the presence of Phase A, an additional phase was also observed. This additional phase is characterizing by scattering peaks at about $q_1 \approx 1.4$, $q_2 \approx 3.0$, and $q_3 \approx 4.5$ nm^{-1} with a repeat distance of about 4.3 nm, indicating the formation of another short periodicity phase (Phase B). The lamellar period of about 4.6 nm is shorter than the 6 nm period of the short lamellar structure observed in the human SC.[3)] This is due to the short chain length of CER[ADS]-C18/C16 used in this study.

Phase separation of FFA and CHOL reportedly occurs in the intercellular lipid model.[15,64)] In pure crystals of PA, a scattering peak is observed at $q = 1.76$ nm^{-1}. In pure CHOL crystals, however, a scattering peak is observed at $q = 1.82$ nm^{-1}. In the scattering patterns of the Models 1 and 2 (Fig. 2 (a)), the peaks are positioned at $q \approx 1.76$ nm^{-1}, and the crystalline PA phase is separated. As-PA has a similar chain length to the fatty acid chain of CER[ADS]-C18/16, PA is particularly poorly compatible with CER[ADS], therefore, phase separation of PA is often observed.[15,64,65)]

In the scattering patterns of Models 2 and 3 (Fig. 2 (a)), the peaks are positioned at $q \approx 1.82$ nm^{-1}, and the crystalline CHOL phase was separated. Other studies have reported that phase-separated CHOL does not affect the multilamellar lipid organization. [15)] In our SAXS profiles at 25°C, two peaks were observed at $q \approx 1.36$ nm^{-1} and $q \approx 1.48$ nm^{-1}, indicating that Phases A and B coexist with crystalline PA and CHOL (Fig. 2 (a)). In WAXD profiles of Models 1 and 2 at 25°C, two peaks are observed at $q \approx 15$ and 17 nm^{-1}, indicating that Orth and Hex coexist (Fig. 2 (b)). On the other hand, in Model 3 (Fig. 2 (b)), no peak was observed at $q \approx 15$ and 17 nm^{-1}, but multiple diffraction peaks were observed at different positions around $q = 13.1$, 13.5, 13.9, and 15.3 nm^{-1}. Accordingly, Phase A and Phase B do not form Orth and Hex in Model 3. Table 1 summarizes the scattering peak position, repeat distance, and phase-separated crystals observed in each model. As indicated in Table 1, in the lipid model using CER[ADS]/CHOL/PA, I found that Phases A and B were observed at any lipid composition ratio. Table 2 summarizes the diffraction peak positions, lattice constant, peak intensities,

sublattices of the diffraction peaks, $R_{Hex/Orth}$ observed in each model. In Table 2, the $R_{Hex/Orth}$ of Model 2 is higher than that of Model 1 i.e. Model 1 has the highest ratio of Orth.

3.2. Changes in X-ray profiles with temperature

Table 2. Composition of Various CER[ADS] Containing Model Lipid Mixtures

Model	Hexagonal (25 °C)		Orthorhombic (25 °C)		HEX/OR peak ratio* (25 °C)
	Peak position (nm^{-1})	Peak intensity (a.u.)	Peak position (nm^{-1})	Peak intensity (a.u.)	
1	15.274	8404.276	17.062	1403.565	1.33
2	15.636	7284.696	17.420	846.288	2.20
3	—	—	—	—	—

Lipid lateral packing is shown. The HEX/OR peak ratio as determined by the Gaussian peak fitting procedure of the WAXD profile at 25°C are also presented.

The SAXS and WAXD data from each model are plotted against temperature in Fig. 3. To analyze the difference in packing structure between Phases A and B, the peaks around $q \approx 1.3$, 1.4, 13.9, 15, and 17 nm^{-1} in the temperature range 25–85°C, I plotted the profiles of intensity I versus the reciprocal spacing q in Fig. 4. Regarding selection of the diffraction peak with $q \approx 13.9$ nm^{-1}, the diffraction peak with the highest intensity at 25°C was selected from among the multiple diffraction peaks shown in Fig. 3 (f). For the peak intensity observed around $q \approx 15$ nm^{-1} (I_{15}), due to the diffraction derived from the Orth and Hex overlap, the value of I_{Hex} (($I_{15} - 2 \times I_{17}$)/3) was used to analyze the diffraction only from Hex.

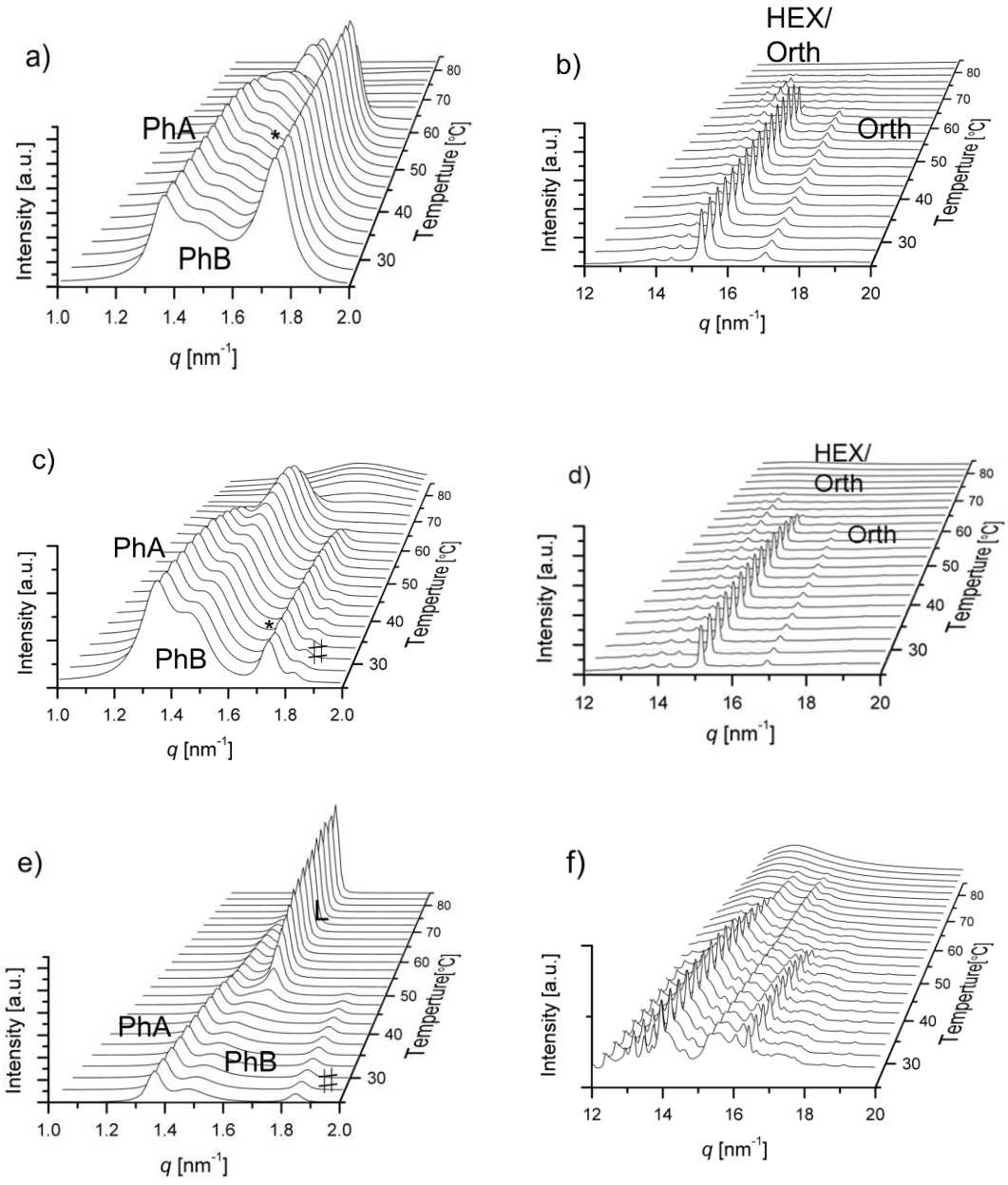

Fig. 3. SAXS and WAXD Profile of Typical CER[ADS]/CHOL/PA Bilayers Belonging to Each Model Monitored at 25–85°C

Data shown are SAXS profiles (left row) and WAXD profiles (right row) of Model 1 (a and b, respectively), Model 2 (c and d, respectively), and Model 3 (e and f, respectively). The peaks originating from the crystalline PA domains are indicated by the asterisk (*). The peaks originating from the crystalline CHOL domains are indicated by the hashtag (#). PhA, Phase A; PhB, Phase B; L, liquid crystal phase.

The peak intensity observed around $q \approx 1.36$ nm^{-1} ($I_{1.3}$) derived from Phase A, which is a short lamellar structure with a lamellar distance of about 4.6 nm, decreases from around 45°C to around 65°C with increasing temperature (Fig. 4 (a) and (c), respectively). Corresponding to the thermal behavior of $I_{1.3}$, the peak intensity observed around $q \approx 15$ nm^{-1} (I_{Hex}) and $q \approx 17$ nm^{-1} (I_{17}) derived from Orth and Hex decreases from around 45°C to around 65°C (Fig. 4 (b) and (d), respectively). In Fig. 5 (a), the peak positions of the scattering peaks observed at $q \approx 1.36$ nm^{-1} in both Model 1 and Model 2 are significantly shifted to the wide-

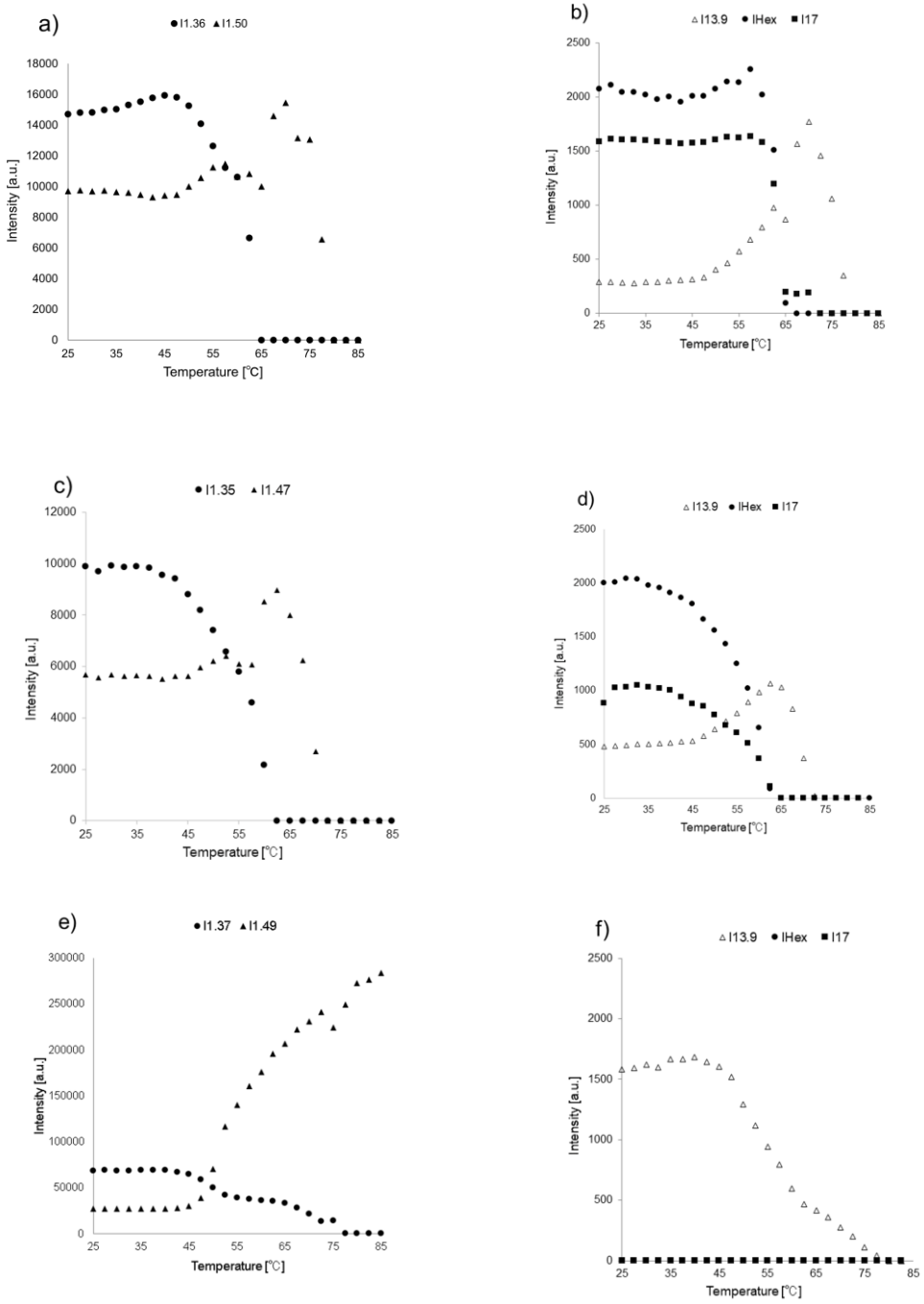

Fig. 4. Changes in X-ray Scattering Peak Intensities of Typical CER[ADS]/CHOL/PA Bilayers Belonging to Each Model as a Function of Temperature at 25–85°

Data shown are SAXS profiles (left row) and WAXD profiles (right row) of Model 1 (a and b, respectively), Model 2 (c and d, respectively), and Model 3 (e and f, respectively). Numbers on the left figures represent parameters of intensity near $q \approx 1.3$ nm^{-1} and $q \approx 1.4$ nm^{-1}, while those on the right represent parameters near $q \approx 13.9$ nm^{-1} ($I_{13.9}$), $q \approx 15$ nm^{-1} (($I_{Hex} : I_{15} - 2 \times I_{17}$) / 3), and $q \approx 17$ nm^{-1} (I_{17}). In Model 3, the scattering peak observed at around $q \approx 1.49$ nm^{-1} is hidden by the strong scattering peak derived from the lamellar liquid crystal near $q \approx 1.54$ nm^{-1} at 45°C and above.

lamellar period. In Models 1 and 2, Phase A seemed to form an Orth and Hex.

In contrast, the peak intensity $I_{1.4}$ observed around $q \approx 1.48$ nm^{-1} derived from Phase B, which is a short lamellar structure with a lamellar distance of about 4.3 nm, correspond to the changes in $I_{13.9}$ as a function of temperature (Fig. 4 (a)−(d)).-In Models 1 and 2, Phase B did not seem to form either Orth or Hex. Souza *et al*. reported a phase (Phase γ in the paper) that is formed at a CHOL ratio of 60% or more in the CER/CHOL binary model and undergoes a phase transition at 75°C with a lamellar period of 4.27 nm.[66] The lamellar period, phase transition temperature, and diffraction peak of this Phase γ and Phase B have similar characteristics. Souza *et al*. reported that multiple diffraction peaks of Phase γ are insufficient to determine the crystalline form of this phase, but the complex diffraction peaks are the result from either lateral phase separation or uneven packing of the layers.[66] The constituent lipids of Phase B are thought to be composed mainly of CER and CHOL. The diffraction peak observed at $q \approx 13.9$ nm^{-1} derived from Phase B has not been focused so far, but in the X-ray diffraction profile of human SC reported by Doucet *et al*., a diffraction peak was observed prominently around $q \approx 13.9$ nm^{-1} in the deep portion of the SC,[50] suggesting that a packing structure similar to Phase B also forms in human SC. Bouwstra *et al*. mentioned that a 4.3 nm phase with a Phase B–like lamellar period was observed in a pilot study on the psoriasis scale in the human SC. [67]

In Model 3 (Fig. 4 (e) and (f)), the peak intensity observed around $q \approx 1.36$ nm^{-1} ($I_{1.3}$) derived from Phase A decreases from around 45°C; however, the decrease in peak intensity is gradual from 55–65°C, and the thermal behavior does not agree with $I_{13.9}$. Moreover, in Fig. 5 (a), the lamellar period of the scattering peak observed around $q = 1.36$ nm^{-1} from Phase A shows that the lamellar period gradually increases from 25–75°C until the peak disappears. In contrast to Models 1 and 2, there was no apparent shortening of the lamellar period associated with a phase transition. I observed that in Phase A of Model 3, lamellar liquid crystals were formed above 25°C. In Model 3, where Phase A does not cause phase transition because it is a lamellar liquid crystal, an increase in intensity was not observed for $I_{1.4}$ and $I_{13.9}$ (Fig. 4 (e) and (f)).

On the other hand, in small angle $I_{1.4}$ observed around $q = 1.49$ nm^{-1} derived from Phase B, the peak position was shifted to $q = 1.54$ nm^{-1} at 45°C or higher, and as the peak

position shifted to q = 1.54 nm^{-1}, an increase in peak intensity was observed and a phase transition to lamellar liquid crystal was observed (Fig. 5 (b) and Fig. 4 (e)). It was difficult to analyze after 45°C, but I assumed that the peak intensity of $I_{1.4}$ in Model 3 also decreased after 45°C as in Models 1 and 2, and the thermal behavior corresponds to $I_{13.9}$.

I found that the packing structure formed in Phase A varies depending on the lipid composition, and that Phase B forms a crystal structure different from Orth and Hex in each model.

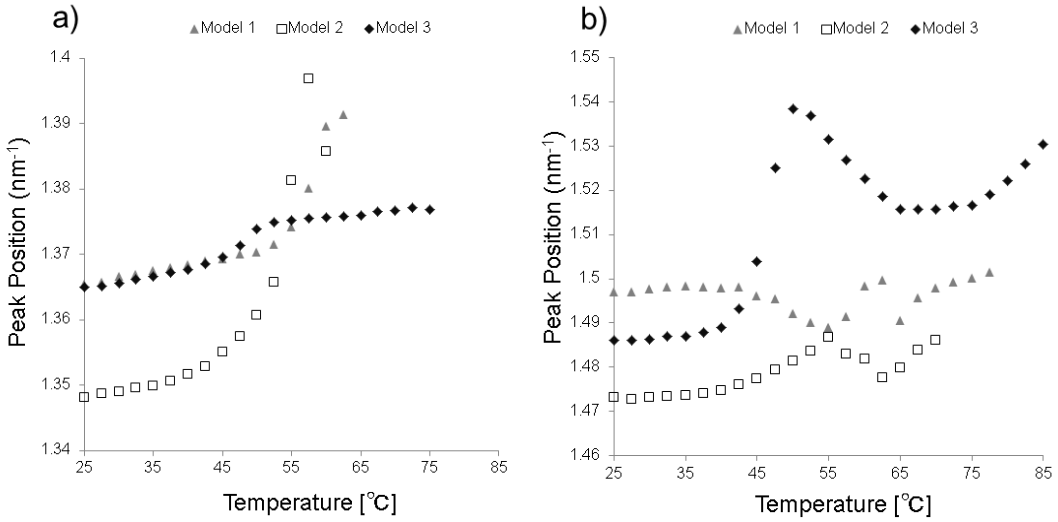

Fig. 5. Changes in the X-ray Scattering Peak Position of Typical CER[ADS]/CHOL/PA Bilayers Belonging to Each Model as a Function of Temperature (25–85°C)

Data shown are parameters for peak positions near q ≈1.36 nm^{-1} (a) and q ≈1.48 nm^{-1} (b) of each model.

3.3. Electron density profile (DECON profile)

Figure 6 shows the calculated electron density profile for each sample. The DECON profile is the average of the data from Phases A and B. The DECON profile rose slowly, increasing from the hydrophobic portion toward the hydrophilic portion and converging on the zero value at r = approx. 2.8 nm (Fig. 6 (a)). The region where the zero value is obtained is thought to coincide with the region where hydration water exists near the hydrophilic part. Since twice the zero value distance exceeds the lamellar periodicity, a hydration layer appears to have formed near the hydrophilic part of the lipid.

The electron density for Model 3 is higher than that for Models 1 and 2 (lower CHOL and CER concentrations) at distances of 1.7–2.2 nm from the hydrophobic group terminus. The electron density of CHOL is reportedly higher than that of hydrophobic chains and equal to that of water. Hence, this indicates that condensed CHOL is localized to the region from the middle part of the hydrophobic groups of intercellular lipids to the vicinity of their hydrophilic groups at distances ranging from 1.7–2.5 nm (Fig. 6 (a)). Although it is not possible to determine the physical properties of the bilayer from the DECON profile alone, it can be inferred that the flexibility of the bilayer is high since CHOL is relatively abundant. These findings support the specificity of Model 3, where Phase A forms lamellar liquid crystals above 25°C, and in Phase B, the transition to the lamellar liquid crystal phase occurs at around 50°C, compared with the other models.

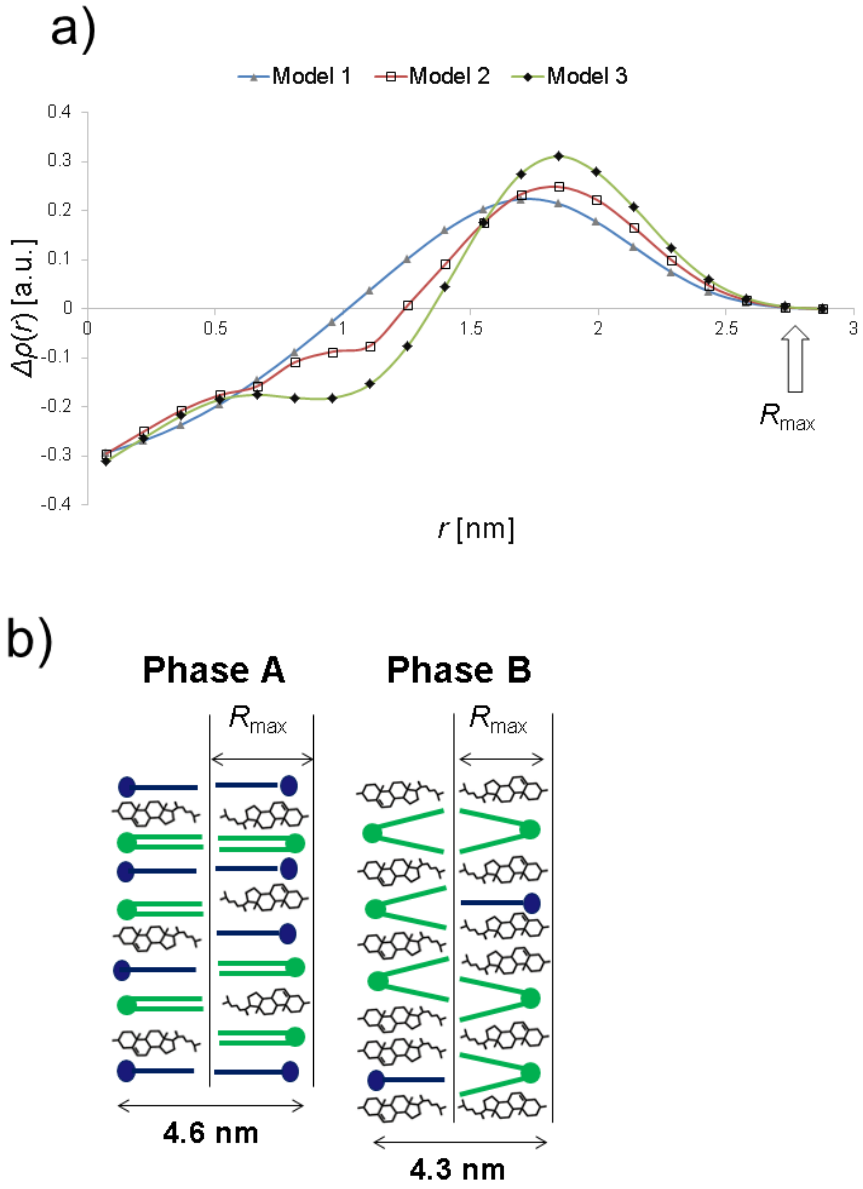

Fig. 6. Electron Density Profile of the Lipid Bilayer for Each Model at 25°C (a)

The r (nm) is estimated from the distance of the bilayer center. Schematic membrane model of Phase A and Phase B for

4. **Discussion**

In this study, I observed Phase A and Phase B structures using an intercellular lipid model (Models 1–3) consisting of the three components, CER[ADS]/CHOL/PA. In interpreting the lamellar periodicity of Phase A, considering that the distance of all-*trans* C–C bonding is 0.127 nm,[68] the maximum chain length of alpha-hydroxy fatty acid is 2.29 nm.[58] The calculated length of the hairpin-shaped CER molecules[57,69] facing each other within a bilayer membrane has a lamellar period of about 4.6 nm, which is the length of the alkyl chains[58] and coincides with the lamellar period of Phase A.

Phase B is thought to correspond to a scattering peak of an unknown 4.3 nm phase in human SC that has a slightly weaker intensity in the vicinity of the scattering peak derived from the main short lamellar structure.[70] Of note, Phase B is present in the human SC, which is presumed to be consistent with lattice defects. The lamellar periodicity of Phase B is shorter than that of Phase A. Given the shorter lamellar periodicity of Phase B, some possible explanations have been proposed in previous reports. Since Phase B has a crystal structure, it is unlikely that its lamellar periodicity is shortened by increasing the fluidity of the alkyl chains. To increase fluidity, the CER may adopt either a partially open alkyl chain form called a V-shaped structure[56,57,64,71–76] or an inclined alkyl chain form.[56] The expected length of the lamellar period for a V-shaped structure is approximately 4.2 nm, which is consistent with our results.

An increase in electron density between 0–0.5 nm in the hydrophobic region of Model 1–3 is not supported by the DECON profile in Fig. 6 (a). The CER conformation of Phase B has been proposed to form a V-shaped structure in each Model, but since an increase in electron density was not observed in the hydrophobic region, I concluded that a distinct intercalation did not form.

From these results, I concluded that the conformation of CER in Phase B observed in this study was a V-shaped structure. The lipid arrangement of Phase A and Phase B is shown in Fig. 6 (b). The lateral packing structure of Phase B indicates that CER[ADS] formed a V-shaped structure, neither Orth nor Hex.

On the other hand, if I focus on the differences between Phase A and Phase B between the three models, Phase A in Model 3 did not form Orth and Hex, unlike in Models 1 and 2. Instead, in Model 3, Phase A formed lamellar liquid crystals above 25°C. I believe that this difference is influenced by the high CHOL ratio in Model 3, but it is difficult to discuss the influence of CHOL concentration in isolation from other factors. CHOL reportedly contributes to the formation of crystal structures over a specific range of CHOL ratio values in the intercellular lipid model, and does not act only in the direction of fluidization.[77] Bouwstra *et al*. reported that liquid crystals are formed by adding FFAs to the intercellular lipid model (CER/CHOL).[78] PA are also thought to contribute to membrane fluidization in Phase A of Model 3. In addition to FFA, the effects of CER saturation and the presence of unsaturated fatty acid chains presumably also affect membrane fluidity. Although our experimental system is different, CHOL acts as a membrane stabilizer for liposomes composed of phosphatidylcholine with unsaturated fatty acids in studies using liposomes. On the other hand, CHOL enhances the membrane fluidity of liposomes composed of phosphatidylcholine with saturated fatty acids.[79,80] Although the molecular structures of phosphatidylcholine and CER are different, the CER[ADS] used in our study is composed of saturated fatty acids, so it is also affected by CHOL and forms a lamellar liquid crystal with high membrane fluidity, thereby reducing membrane stability. Based on the above discussion, I concluded that fluidization is characteristically promoted in Phase A of Model 3 due to the influence of both CHOL and PA at a CER[ADS]/CHOL/PA composition ratio of approximately 1:1:1 (mol/mol).

In Model 3 (Fig. 3(e)), a phase transition of Phase B to the liquid crystal phase is observed at around 50°C, whereas in Models 1 and 2, no such phase transition is observed (Fig. 3 (a) and (c)). Models 1 to 3 have different lipid compositions in Phase B. Although the constituent lipids of Phase B are thought to be mostly CER and CHOL, the CHOL ratio is higher in Phase B of Model 3 as the phase transition to lamellar liquid crystals occurs at around 50°C. On the other hand, Phase B in Models 1 and 2 is thought to be composed mainly of CER and CHOL, but has a characteristically low CHOL ratio and characteristically high CER ratio. Moreover, Phase B in Models 1 and 2 does not undergo a phase transition to lamellar liquid crystals.

To investigate the relationship between the skin's barrier function and short FFA species,[31] I used PA in our study. The presence of a small amount of FFA with a short chain length of either C_{16}, C_{18}, or C_{20} in the intercellular lipid model （CER[NS] or CER_{mix}/CHOL/FFAs : 1/1/1, mol/mol） decreases the conformational order of the intercellular lipid model and increases its permeability.[81]

PA can weaken intermolecular interactions in the non-polar region depending on its abundance.[53] With regards to the packing structure, studies focused on the phase transition temperature[53] and order parameter[56] have found that CER species containing non-hydroxy fatty acids have a denser structure than those with an alpha-hydroxyl group.

CER[AS] having an alpha-hydroxy group has a positive correlation with TEWL.[11] The V-shaped structure was verified in this study which formed in the intercellular lipid model using a combination of CER[ADS] with an alpha-hydroxy group and PA as a short-chain FFA. The V-shaped structure may occur commonly in the CER subclasses containing an alpha-hydroxy group.

The abundance of short FFAs is increased in damaged skin,[31] and in the skin of patients with atopic dermatitis, which have a shorter lamellar structure than healthy skin.[11] Hereafter, it is necessary to verify whether the V-shaped structure is formed by the combination of CER containing alpha-hydroxy FFA subclasses and FFA of short chain length in actual skin.

In order to maintain barrier function, it is important to understand differences in the lateral packing of intercellular lipids. In this study, I proposed that the combination of CER[ADS] and PA as a short-chain FFA species, could cause the CER conformation to adopt a V-shaped structure. This structure is neither Orth nor Hex, but another crystal structure, possibly a monoclinic crystal. The lamellar structure with a lamellar period of about 4.2 nm, which was conventionally considered as an unknown phase, is considered to be a phase formed mainly of CER and CHOL, in which a CER forms a V-shaped structure similar to Phase B.

I found that temperature scanning simultaneous SAXS and WAXD measurement is a powerful tool for studying the difference in the characteristics of the packing structures. Using

this method, I have elucidated the different lamellar periods between Phases A and B for the first time.

Further experiments using membrane transport experiments and temperature scanning FT-IR measurements will provide a well-defined packing structure for Phase B and clarify its relationship with barrier function. In the future, I will consider how the composition of CER subclasses and shorter fatty acid chains in the packing structure reduce barrier function. In addition, a comprehensive understanding that includes CER biosynthetic pathways is required to clarify the effect of different CER subclasses on the barrier function of intercellular lipids. I intend to pursue such studies and propose measures to control CER conformations in order to learn how the barrier function of intercellular lipids can be enhanced.

5. **Conclusions**

In the intercellular lipid model using short chain FFA and CER[ADS], two kinds of lamellar structures with different lamellar periods, Phase A and Phase B, were formed. Hydrocarbon chain packing of Phase B formed neither Orth nor Hex regardless of the lipid composition. Our results also suggest that Phase B had a V-shaped CER conformation which formed a crystal structure. This means that an increased ratio of short chain FFA in FFA species led to the malformation of a lamellar structure with a low Orth ratio that would reduce barrier function. These differences in lamellar periods and hydrocarbon chain packing are thought to be caused by differences in CER conformations. Barrier function may be enhanced by controlling the ratio of CER subclasses and the conformation of CER. The combination of FFA chain length and CER subclasses are the key.

CHAPTER 2

Distribution of domains formed by lateral packing of intercellular lipid in the stratum corneum

1. Introduction

Intercellular lipids in the SC protect the body from allergens and pathogens and inhibit water evaporation, thereby serving as a barrier. Intercellular lipids are composed of CERs, and FFAs.[82] Intercellular lipids exert their barrier function by forming a characteristic lamellar structure[8] consisting of orthorhombic and hexagonal packing structures and liquid crystals.[9,83] A study involving electron diffraction measurement reported different domain sizes of orthorhombic and hexagonal packing structures.[10] Additionally, the proportion and distribution of the crystalline and liquid-crystalline structures are considered to affect barrier function. A relationship between the packing structure and TEWL value was proposed based on the phase transition behavior of intercellular lipids.[84] To assess the skin barrier, it is important to clarify the microdomain distribution within the packing structures rather than the averaged information.

In the past, X-ray diffraction and electron diffraction were used to analyze the crystal structure of the packing structure, whereas the analysis of the liquid crystal was difficult because of the influence of keratin-derived diffraction.[7,50] More recently, however, the packing structure of intercellular lipids, including liquid crystals, has been analyzed by Fourier transform IR spectroscopy (FTIR). Differences in packing structure were evaluated by confirming the shift of the peak derived from CH_2 symmetric stretching vibration of the alkyl chains of intercellular lipids.[83,85] Imaging analysis of the packing structure of SCs has been performed in vertical SC cross sections by transmission FTIR.[86] In addition, Raman spectroscopy was used to evaluate the planar distribution of packing structures in intercellular lipid models.[44,87,88] However, the horizontal distribution of the packing structure of intercellular lipids in the SC has not been examined.

Further clarification of the distribution and proportions of domains formed by orthorhombic and hexagonal packing structures and liquid crystals in the human SC will help

identify the relationship between the proportion of each constituent and TEWL, an index of barrier function. This approach will contribute to the development of more effective skin care products that improve barrier function. In this study, I used focal plane array (FPA)-based FTIR imaging technology[89] to analyze the shift of the CH_2 symmetric stretching vibration-derived peak around 2850 cm^{-1} and thus calculate the distribution and proportions of domains formed by packing structures in SC cell units. The distribution was analyzed using human SC samples from high- and low-TEWL skin. The correlation between this distribution and the lipid composition of CERs was determined using electrospray ionization tandem mass spectrometry (ESI-MS/MS)-based shotgun lipidomics. Recently, the chain length distributions of FAs and sphingoid bases of CERs have been reported.[30,90–92] However, the relationship between these distributions and TEWL remains unclear. I therefore also analyzed CER subclasses and their carbon chain lengths.

2. Experimental

2.1. Materials

Methanol, propan-2-ol, chloroform, acetyl chloride, and ammonium acetate were of analytical grade. Deuterated CER[NS] D3 (36:1;2, [sum of carbon atoms in long-chain bases (LCBs) and FAs]:[sum of double bonds in LCBs and FAs];[sum of hydroxyl groups in LCBs and FAs] (cat# 2201) was purchased from Matreya LLC (State College, PA, USA). *N*-tricosane (cat#91447, purity >99.5%) were purchased from Supelco (Bellefonte, PA, USA). Calcium fluoride plates were provided by Japan High Tech (Fukuoka, Japan).

2.2. Skin sampling

All sampling from human subjects was performed with informed consent in accordance with the Declaration of Helsinki after approval by the Bioethics Committee of Interface, Inc. (Akita, Japan) (decision number IF19-037). Exclusion criteria were as follows: current or prior skin diseases, current allergic diseases, current medication use, pregnancy, and exposure to UV radiation in a context other than daily activities. Human skin SCs were obtained from 36 healthy Japanese female donors between the ages of 25 and 69 years. Subjects washed the skin surface of the cheek area with cleansing gel and creamy soap. After washing, subjects spent at least 15 minutes in a thermo-hydrostatic chamber at 20 °C and 50% humidity. All SC samples were prepared as described in Sadowski .[29)]

The SC sampling site for tape stripping was the middle of the left cheek. To prevent any influence by factors such as washing or cosmetics application, the uppermost SC layer was removed twice with D-Squame tape (D100, CuDerm corporation, Dallas, TX, USA). Then, a third stripping was performed, and the SC sample was used for lipid quantification analysis.

Copper grids (Thin Bar Grid, Gilder Grids Ltd., Grantham, UK) (cat# G2200C or cat# G2650C: 200 or 600 mesh) for electron microscopy coated with acrylic adhesive (POLYTHICK, Sanyo Chemical Industries, Ltd., Kyoto, Japan) were used to obtain SC cells with intact

intercellular lipids. Grids with the adhesive applied only to the copper frame portion were made by applying a POLYTHICK / ethyl acetate (1:3) solution, absorbing the excess solvent with filter paper, and drying. To collect SC cell samples after three stripping sessions with D-squame tape, a grid was pressed on the sampling site for 5 seconds and removed to store the SC cells attached to the grid. SC cells within the cheek area of six subjects, described below, were collected according to the protocol. Five SC cells were analyzed per subject.

2.3. Transepidermal water loss measurements to determine barrier function

TEWL was measured using a Vapometer (SWL5001JT, Delfin Technologies Ltd., Kuopio, Finland). Three measurements were performed at the center of the left cheek, in adjacent locations to prevent overlap.

2.4. Skin conductance

Skin conductance was measured using a SKICON-200EX (Yayoi Co. Ltd., Tokyo, Japan). Five adjacent measurements were performed in the same location as the TEWL assessment. The lowest and highest values were excluded, and the remaining three values were used for statistical analysis.

2.5. FTIR imaging measurements

From a total of 36 subjects, the five with the highest TEWL and the five with the lowest TEWL were selected. The three subjects with the highest TEWL and lowest SC water content *in vivo* and the three with the lowest TEWL and the highest SC water content *in vivo* were then chosen for analysis. Subject Nos. 11, 37, and 45 comprised the high-TEWL group, while Subject Nos. 18, 19, and 44 comprised the low-TEWL group. The domains formed by packing structure distribution of SC intercellular lipids in the grids was measured by FPA-based FTIR imaging. The instrument used was a Hyperion3000 FTIR microscope combined with a Vertex70 Fourier transform infrared spectrometer (Bruker Optik GmbH, Ettlingen, Germany). The microscope was equipped with a 36x Cassegrain objective and a 64 x 64 mercury cadmium

telluride FPA detector with 2 μm pixel resolution. SC cell samples with the widths of 30−80 μm were analyzed in transmission mode. The samples were scanned 64 times in the spectral range of 900−3900 cm^{-1} with a resolution of 4 cm^{-1}, and the average spectrum was analyzed. The domains formed by packing structure was determined according to the shift of the peak position derived from CH_2 symmetric stretching vibration, which was inferred from the center of gravity of the peak.[20] FT-IR data were processed and analyzed using the OPUS 7.2 software suite (Bruker Optik GmbH).

First, I validated whether the phase transition of *n*-tricosane, which is well known to be characterized by thermotropic phase behavior,[83,94–96] could be detected using the position of the CH_2 symmetric stretching band. This alkane has been found to exist in four different phases: orthorhombic, face-centered orthorhombic (FCO) or pseudo-hexagonal, hexagonal, and liquid crystal, in the temperature range of 28−51 °C with phase transition temperatures of 40.4 °C, 45.8 °C, and 47.6 °C, respectively.[23] *n*-Tricosane was measured under the same conditions as for SC cells. To collect spectra from *n*-tricosane, a small amount of powder was placed between the calcium fluoride plates (the thickness of *n*-tricosane was less than 2 μm). Prepared plates were set on an automatic heating stage (10036, Linkam Sci. Instr., Tadworth, UK). In the temperature studies, the *n*-tricosane plates were heated at the rate of 1 °C/min, and spectra were collected at 1 °C increments between 28 and 51 °C. The temperature was maintained while each spectrum was collected.

Figure 7 shows a bright-field image of SC cells in the grid and an image of the incident infrared light on the sample. The distribution of the domains formed by intercellular lipid packing structure was analyzed for five SC cells per subject.

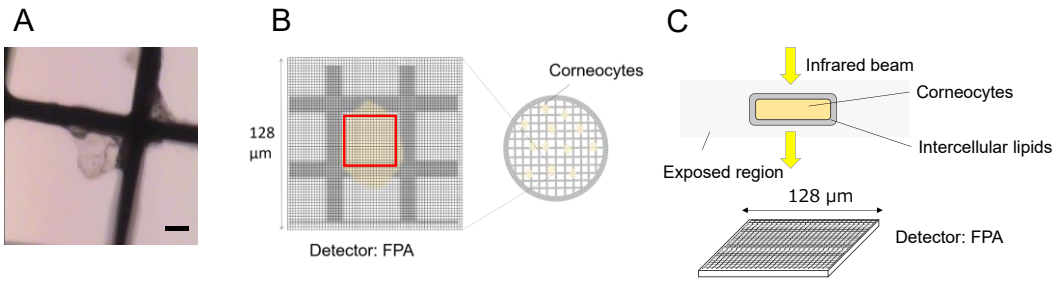

Fig. 7. Incidence of IR Radiation on a Sample in FPA-Based FTIR Imaging Measurements

(A) Bright field image of optical micrograph of SC cells attached to the frame of a copper grid for electron microscopy. The SC cell layer was stripped from the surface of human skin by the grid stripping method, then FPA-based FTIR imaging was performed. Bar indicates 20 μm. (B) Top-view image of the FPA detector. When irradiated with infrared light and detected by a 64 × 64 FPA detector with 128 μm per side, pixel information with a resolution of 2 μm is obtained. The distribution of the domains formed by packing structure of hydrocarbon chains of intercellular lipids on SC cells was identified. The red frame indicates the analysis area. (C) Side-view image when infrared light is incident on the sample.

2.6. Quantification of CERs by ESI-MS/MS-based shotgun lipidomics

The nonacyl-CER content of tape-stripped SCs from the high- and low-TEWL groups was examined by ESI-MS/MS-based shotgun lipidomics.[29,97,98] Acyl-CERs were excluded because the ionization methods are different, and it is therefore difficult to compare the results to those of nonacyl-CERs. Samples for CER analyses were prepared from the third strip of tape. SCs were extracted from tape strips, then analyzed and quantified as follows, using the method described in Sadowski *et al*.[29]

Samples were injected directly into a QExactive mass spectrometer (Thermo Fisher Scientific, Waltham, MA, USA) equipped with a TriVersa NanoMate ion source (Advion

Biosciences, Ithaca, NY, USA), and immediately analyzed in both positive and negative ion modes with a resolving power of $R_{m/z=200}$ = 280000 for MS and $R_{m/z=200}$ = 17500 for MSMS. MSMS fragmentation was performed at 35% normalized collision energy and was triggered by an inclusion list covering the corresponding MS mass ranges.[99] Combining both MS and MSMS data, all CER subclasses were monitored as acetate adducts. The previously reported precursor ions and confirmatory MSMS fragments[25,29,97,98] are summarized in Table S1.

An internal standard of 14 pmol CER[NS] D3 36:1;2 (18:1;2, 18:0;0) per sample was used in this study because CER[NS] is not natively present in skin samples. Quantification was performed by normalizing the isotopically corrected intensity of the monoisotopic peak of each native species to the isotopically corrected intensity of the monoisotopic peak of the internal standard. The amounts of CER molecular species were calculated from the ratios of characteristic MSMS fragments, as described previously.[99] Nonacyl-CERs were normalized by deuterated CER[NS].

CERs are divided according to subclass and chain length.[46] Figure S1 shows that differences between the 8 CER subclasses are due to varying combinations of two types of acyl chains (non-hydroxy and alpha-hydroxy) and the acid-amide bonds of four types of sphingoid bases (dehydrosphingosine, sphingosine, phytosphingosine, and 6-hydroxyl).[25,100] Quantitative data were used to calculate the total amount of nonacyl-CERs (pmol/μg (the amount of protein)) and the percent of each CER amount relative to the total nonacyl-CER amount (%). A Squamescan 850A (Heiland Electronic GmbH, Wetzlar, Germany) was used to determine the amount of protein in SCs. The amount of protein for correction was calculated based on the regression equation optical density (OD) = 0.623x + 2.703 (R = 0.85), following the method of Voegeli *et al*.[101]

2.7. Lipid extraction

A tape-stripped sample containing one stripping disc was placed in a 2 mL

polypropylene tube, and 900 μL of methanol containing an internal standard was added for lipid extraction. Samples were shaken at 4 °C and 1400 rpm for 1 hour. The extract was then transferred to a multi-well plate and dried in a speed vacuum concentrator. The dried extracts were resuspended in an acquisition mixture of 7.5 mM ammonium acetate in chloroform:methanol:propan-2-ol (1:2:4, V:V:V). All liquid handling steps were performed using a Hamilton Robotics STARlet robotic platform equipped with Anti Droplet Control for pipetting of organic solvents.

2.8. Data analysis

Welch's *t*-test with Bonferroni's multiple comparison was used to analyze the difference in the proportions of domains formed by packing structures between the high- and low-TEWL groups. Welch's *t*-test was used to analyze skin parameters, total amount of CER, and the average data from studies of packing structures. Two-way ANOVA was performed to analyze quantitative data on subclass distribution and chain length distribution of CERs. The significance level for rejection of the null hypothesis was set at $p < 0.05$.

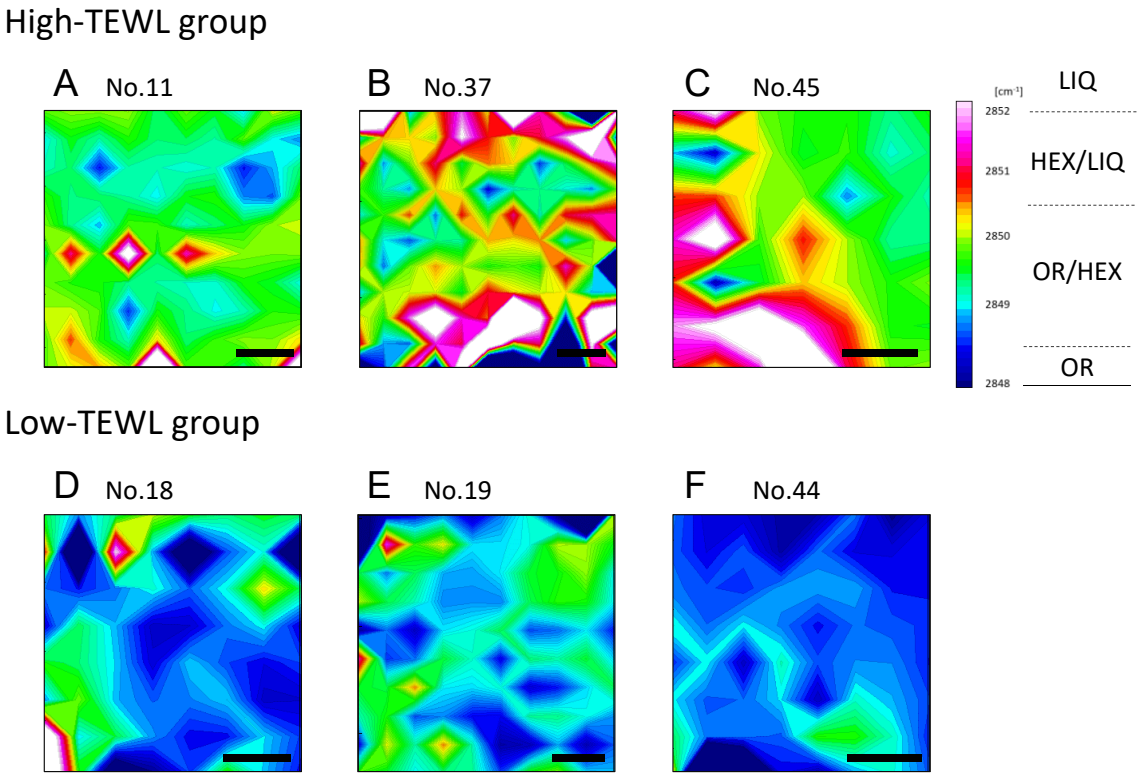

Fig. 8. FPA-Based FTIR Imaging Results Showing Intercellular Lipids in SCs from Each Subject

The upper row indicates the high-TEWL group: (A) subject No. 11, (B) subject No. 37, and (C) subject No. 45. The lower row indicates the low-TEWL group: (D) subject No. 18., (E) subject No. 19., and (F) subject No. 44. Based on the spectral information derived from intercellular lipids, the domains formed by packing structure is mapped by color according to the position shift information of the peak derived from the CH_2 symmetric stretching vibration for approximately 70 spectra detected by the FPA detector. Each domains formed by packing structure is shown according to the color bar. The white domain indicates a region larger than 2852 cm^{-1}. Bar indicates 5 μm. OR, mainly orthorhombic packing domain; OR/HEX, mainly orthorhombic and hexagonal packing domain; HEX/LIQ, mainly hexagonal and liquid crystal domain; LIQ, mainly liquid crystal domain.

3. Results

3.1. Skin parameters

Table 3 shows the skin parameters of the six selected subjects: Subject Nos. 11, 37, and 45 had high TEWL values (high-TEWL group) and Subject Nos. 18, 19, and 44 had low TEWL values (low-TEWL group). The skin of the high-TEWL group had a low moisture value while that of the low-TEWL group had a high moisture value. The skin parameter results of all subjects are shown in Table S2.

Table 3. Summary of Skin Parameters

Group	High-TEWL			Low-TEWL			Means ± S.D.		*p*-Value (High-TEWL *vs.* Low-TEWL)
Subject No.	No. 11	No. 37	No. 45	No. 18	No. 19	No. 44	High-TEWL	Low-TEWL	
Age	24	45	25	63	69	48	31.3 ± 11.8	60.0 ± 10.8	0.036*
TEWL (g/m^2/h)	15.6 ± 0.5	21.6 ± 0.1	16.2 ± 0.2	7.4 ± 0.3	7.5 ± 0.1	7.5 ± 0.4	17.8 ± 3.3	7.5 ± 0.1	0.032*
Skin conductance (μS)	85.0 ± 6.2	47.7 ± 7.5	91.0 ± 7.8	176.7 ± 4.6	189.0 ± 14.4	156.3 ± 21.4	74.6 ± 23.5	174.0 ± 16.5	0.005**
Total amount of nonacyl-CERs (pmol/μg)	276	278	201	197	373	418	251.4 ± 25.1	329.3 ± 67.5	0.459
Mean FTIR symmetric stretching peak position (cm^{-1})	2849.4 ± 1.7	2850.0 ± 2.1	2849.7 ± 0.9	2848.5 ± 3.0	2849.1 ± 0.9	2848.7 ± 0.7	2849.7 ± 0.3	2848.8 ± 0.3	0.021*

TEWL (mean ± standard deviation (S.D.)), skin conductance (mean ± S.D.), CER quantification results, averaged packing structure information, and the results of Welch's *t*-test comparing the high- and low-TEWL groups are summarized. [*(p< 0.05), ** (p< 0.01)]

3.2. Thermotropic phase transitions of *n*-tricosane

Figure S2 shows the results for the thermotropic behavior of the position of the CH_2 symmetric stretching mode of *n*-tricosane. These phase transitions were clearly indicated by the temperature dependence of the magnitude of the position of the CH_2 symmetric stretching vibration with respect to the orthorhombic-FCO and hexagonal-liquid crystal phase transitions, except for the FCO-hexagonal phase transition. Within the orthorhombic phase (28–40 °C), the CH_2 symmetric stretching mode was centered at 2848.4 cm^{-1}. Within the FCO and

hexagonal phases (41–47 °C), the CH_2 symmetric stretching mode was centered at 2850.3 cm^{-1}. In the liquid crystal phase (48–51 °C), the CH_2 symmetric stretching mode reached a plateau at 2852.3 cm^{-1}.

3.3. Analysis of the distribution of domains formed by intercellular lipid packing structure based on FPA-based FTIR imaging

Figure 8 shows a representative example of domains formed by packing structure distribution according to FPA-based FTIR imaging of SC cell samples. Based on the shift of the peak position due to the phase transition of *n*-tricosane, peak position values less than 2848.4 cm^{-1} were identified as mainly orthorhombic packing domain (OR), those between 2848.4 cm^{-1} and 2850.3 cm^{-1} were identified as mainly orthorhombic and hexagonal packing domain (OR/HEX), those between 2850.3 cm^{-1} and 2852.3 cm^{-1} were identified as mainly hexagonal and liquid crystal domain (HEX/LIQ), and those larger than 2852.3 cm^{-1} were identified as mainly liquid crystal domain (LIQ) with high fluidity. The deep blue areas show OR, the red areas show HEX/LIQ, and the white areas show LIQ. The distribution of packing structures was not uniform, resulting in domain formation. Typical IR spectra of OR, HEX, and LIQ are shown in Figure S3.

Table S3 shows the number of pixels analyzed in five independent SC cells per subject. FPA-based FTIR imaging was carried out to determine the distribution of domains formed by intercellular lipid packing structures. Figure 9 shows the proportions of domains formed by packing structures in each group. The average FTIR symmetric stretching peak positions

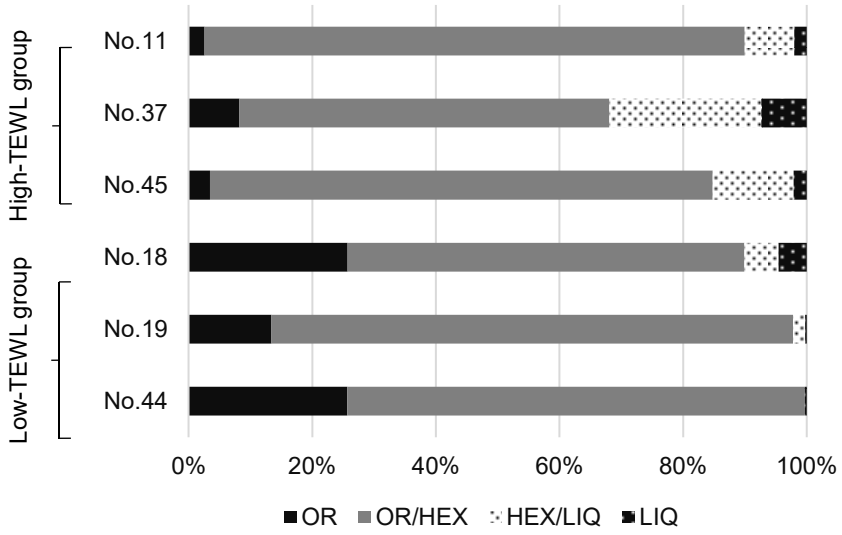

Fig. 9. Proportions of Domains Formed by Intercellular Lipid Packing Structures in SCs Based on FPA-Based FTIR Imaging Measurements

The top and bottom three columns represent the high-TEWL and low-TEWL groups, respectively. Proportions are shown from left to right as OR, OR/HEX, HEX/LIQ, and LIQ. Five SC cell samples were collected from each subject by grid stripping, and the proportions of domains formed by packing structures were confirmed based on information from a total of about 350 spectra. OR, mainly orthorhombic packing domain; OR/HEX, mainly orthorhombic and hexagonal packing domain; HEX/LIQ, mainly hexagonal and liquid crystal packing domain; LIQ, mainly liquid crystal domain.

calculated from all the pixels in each subject are shown in Table 3. The peaks were approximately 2849.7 cm^{-1} in the high-TEWL group and approximately 2848.8 cm^{-1} in the low-TEWL group. The mean value of the FTIR symmetric stretching peak positions differed significantly between the two groups.

Figure 10 compares the peak proportion of each domain between the two groups. The number of pixels attributed to OR, counted at wavenumbers below 2848.4 cm^{-1}, was significantly higher in the high-TEWL group than in the low-TEWL group. The number of pixels for OR/HEX, counted at wavenumbers between 2848.4 cm^{-1} and 2850.3 cm^{-1}, showed no significant difference between the two groups, but this domain had the largest proportion. The low-TEWL group had an OR proportion ranging from 3–8%, whereas the high-TEWL group had an OR proportion ranging from 13–26%. The maximum proportion of liquid crystals was

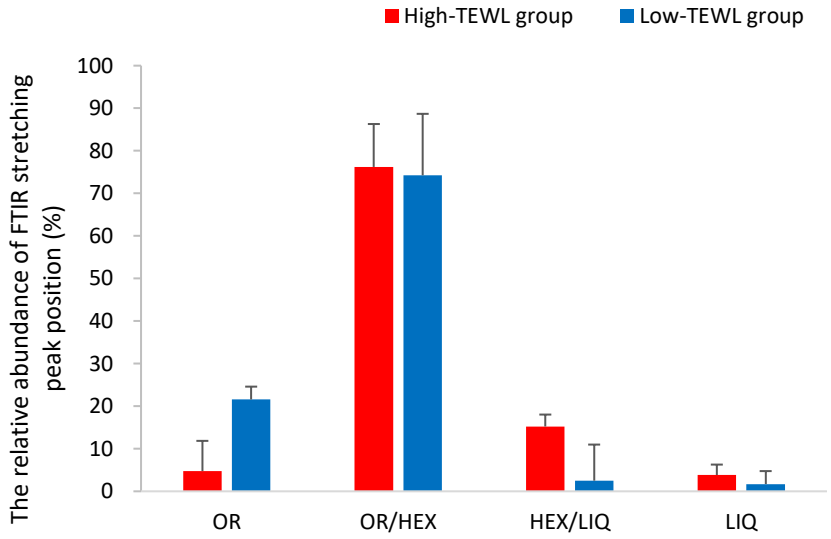

Fig. 10. Differences in the Proportions of Domains Formed by Packing Structures between High- and Low-TEWL Groups

SC cells containing intercellular lipids were collected from the high- and low-TEWL groups and analyzed by FPA-based FTIR imaging. Peak position values below 2848.4 cm^{-1} are classified as OR, those between 2848.4 and 2850.3 cm^{-1} as OR/HEX, those between 2850.3 and 2852.3 cm^{-1} as HEX/LIQ, and those above 2852.3 cm^{-1} as LIQ. From left to right, comparisons of the OR, OR/HEX, HEX/LIQ, and LIQ proportions are shown. Welch's t-test results showed significant differences between groups for OR proportion. Data are presented as means ± S.D., $n = 3$. [* ($p < 0.05$)]. OR, mainly orthorhombic packing domain; HEX/LIQ, mainly hexagonal and liquid crystal packing domain; LIQ, mainly liquid crystal domain.

estimated to be about 32% in high-TEWL skin and about 10% in low-TEWL skin. The proportion of domains containing LIQ in intercellular lipids is relatively small, and the crystalline phase, OR/HEX, constitutes the major domain at 60–80%.

3.4. Lipid identification and quantification

To evaluate differences in CER composition, the quantitative results for each CER subclass are shown in Figure 11. Two-way ANOVA of CER composition in the high- and low-TEWL groups showed no significant difference. I compared the lipid composition of each CER subclass according to chain length. CERs consist of sphingoid chains and FA chains joined by amide bonds (Fig. S1), and the lipid compositions of these components were determined.

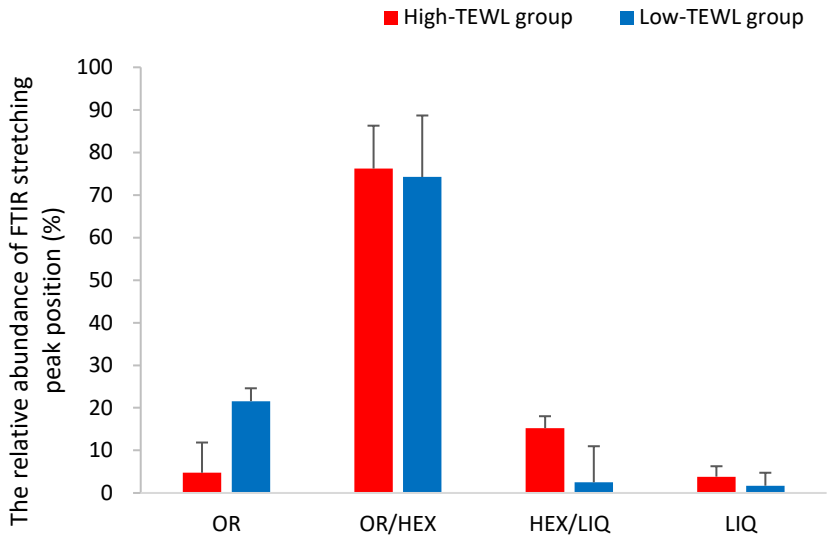

Fig. 11. Differences in CER Composition between the High- and Low-TEWL Groups

ESI/MS/MS-based shotgun lipidomics was used to analyze the lipid composition of CERs in SC samples collected from the two groups by tape stripping, and the quantitative results were compared among the nonacyl-CERs. The red columns show the mean values of the three subjects in the high-TEWL group, and the blue columns show the mean values of the three subjects in the low-TEWL group. Two-way ANOVA results showed no significant differences in the distribution of the quantitative values among subclasses. Data are presented as means ± standard error (S.E.), $n = 3$.

Table 4 shows the results of two-way ANOVA of CER chain length distribution between the high- and low-TEWL groups. Significant differences in C-chain distribution were observed for CER[NP], CER[ADS] (ADS = alpha-hydroxy-dihydrosphingosine), and CER[AP] (AP = alpha-hydroxy-phytosphingosine). Although not significantly different, a trend toward more CER[AS] was observed in the high-TEWL group. Significant differences in the S-chain were observed for CER[NP], CER[ADS], and CER[AP].

Table 4. Summary of the Comparison of the Chain Length Distributions of CER Subclasses

CER subclass	*p*-Values	
	C-chain	S-chain
CER [NDS]	0.475	0.547
CER [NS]	0.824	0.908
CER [NP]	0.041*	0.026*
CER [NH]	0.100	0.196
CER [ADS]	0.005**	0.003**
CER [AS]	0.050	0.165
CER [AP]	0.026*	<0.001**
CER [AH]	0.491	0.545

The chain length distribution of the C-chain and S-chain of the eight subclasses of nonacyl-CERs were compared between the high- and low-TEWL groups by two-way ANOVA. [*($p< 0.05$), ** ($p< 0.01$)]

Figure 12 shows the proportions of FA chains by chain length in CER subclasses containing alpha-hydroxy groups. The proportions of C16, C24, and C26 FA chains were higher than those of other molecular species in CER[AS], and were greater in the high-TEWL group. The proportion of C24 FA chains was higher than those of other molecular species in CER[AP], and was greater in the high-TEWL group. On the other hand, CER[ADS] was less abundant than other alpha-hydroxyceramide subclasses, but it showed a broad distribution of FA chains with high proportions of C24 to C27, including odd-numbered chains, and most proportions were lower in the high-TEWL group. The proportions of the contents of S-chain

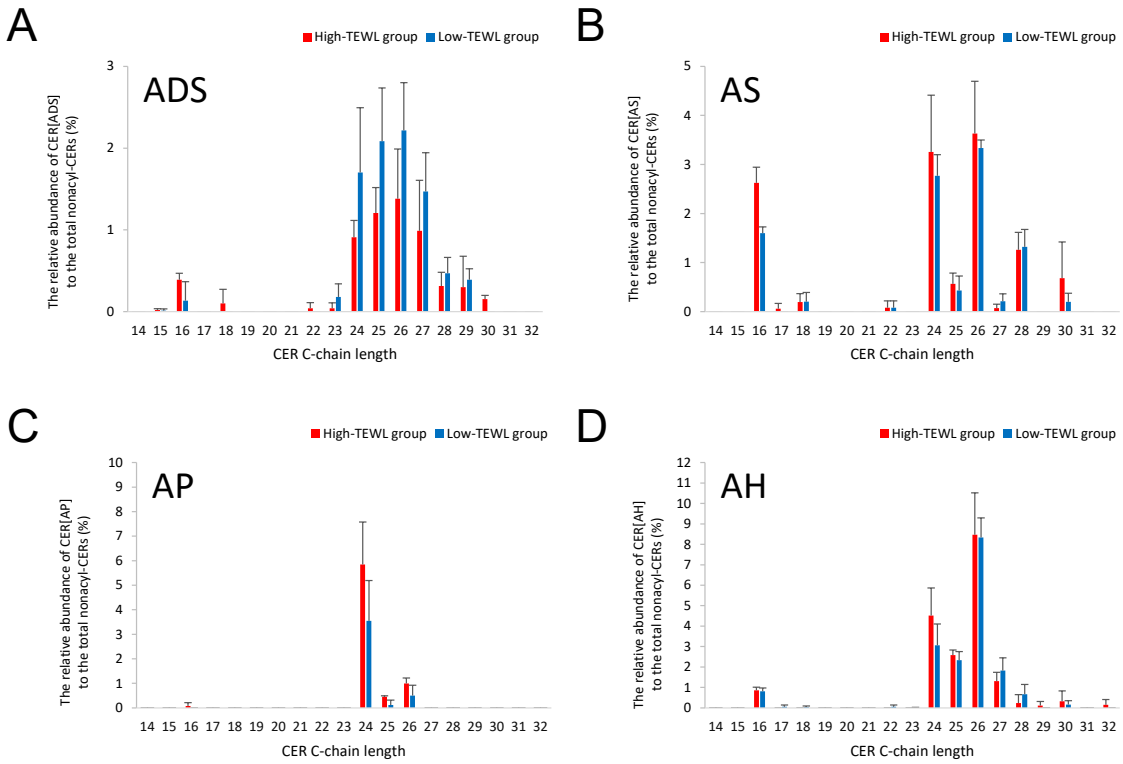

Fig. 12. Proportions of FA Chains According to Chain Length in CER Subclasses Containing alpha-Hydroxy Groups

The relative abundance of each CER to the total nonacyl-CERs (%) was quantified by ESI/MS/MS-based shotgun lipidomics. (A) CER[ADS], (B) CER[AS], (C) CER[AP], (D) CER[AH]. Data are presented as means ± S.D., $n = 3$.

species by chain length are shown in Figure 13. In the S-chain, the proportion of C18 FA chains that were not elongated was higher than the proportions of other molecular species in CER[AS] and CER[AP], whereas the proportion of C18 FA chains was increased in the high-TEWL group compared to the low-TEWL group. Although no significant difference in CER[AH] (AH = alpha-hydroxy-6-hydroxysphingosine) was observed between the high- and low-TEWL groups, the proportion of C18 FA chains was higher in the high-TEWL group.

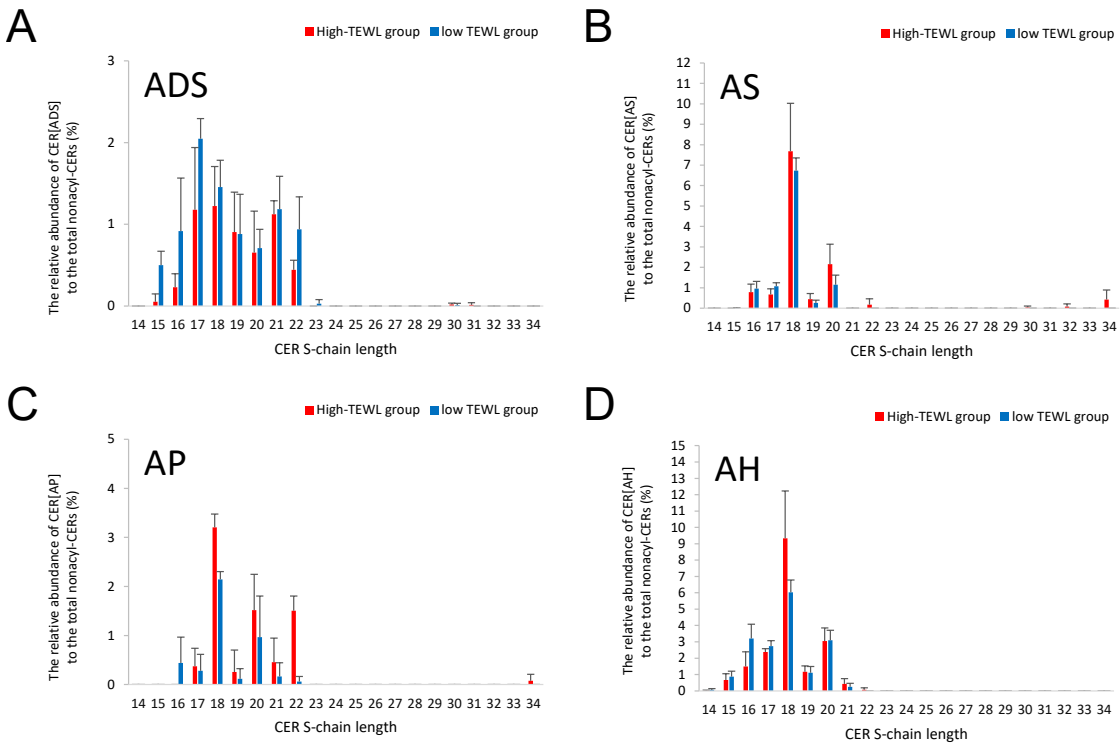

Fig. 13. Proportions of Sphingoid Bases According to S-Chain Length in CER Subclasses Containing alpha-Hydroxy Groups

The relative abundance of each CER to the total nonacyl-CERs (%) was quantified by ESI/MS/MS-based shotgun lipidomics. (A) CER[ADS], (B) CER[AS], (C) CER[AP], (D) CER[AH]. Data are presented as means ± S.D., $n = 3$.

Figure 14 shows the proportions of FA chains by chain length in CER subclasses containing non-hydroxy groups. The proportions of C24 and C26 FA chains were higher than those of other molecular species in CER[NP], and were greater in the low-TEWL group. The proportions of the contents of S-chain species by chain length are shown in Figure 15. In the S-chain, the proportions of C16, C17, and C18 FA chains that were not elongated were greater in the low-TEWL group.

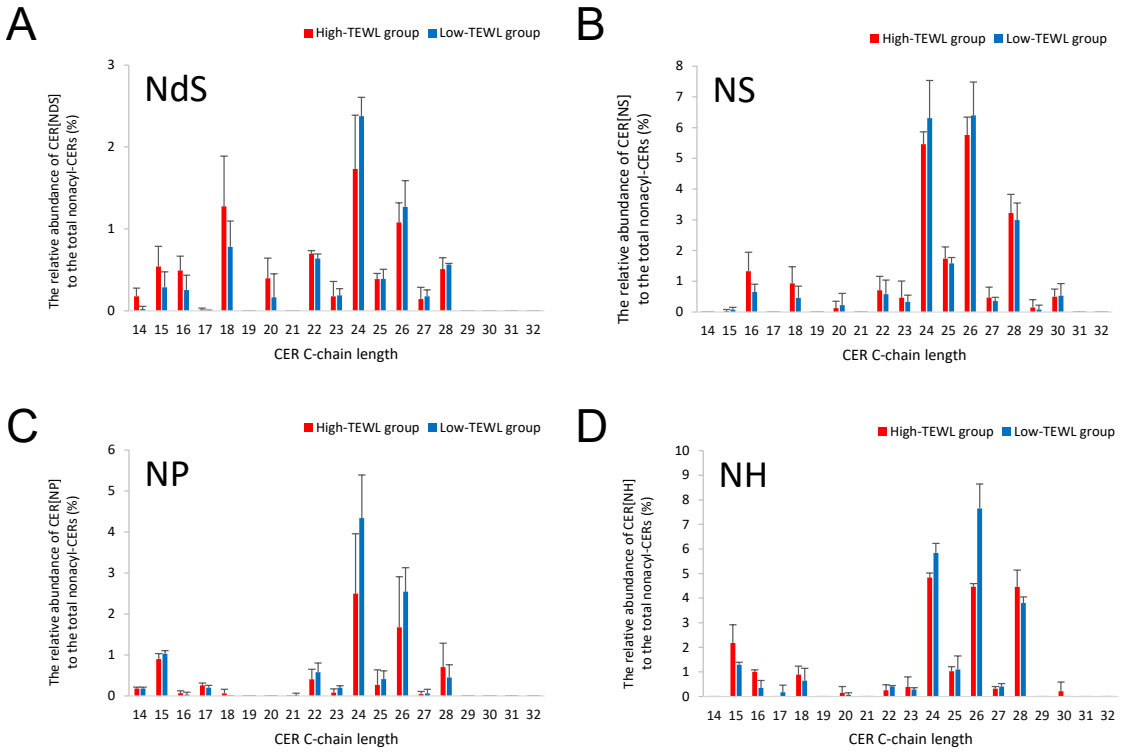

Fig. 14. Proportions of FA Chains According to Chain Length in CER Subclasses Containing alpha-Hydroxy Groups

The relative abundance of each CER to the total nonacyl-CERs (%) was quantified by ESI/MS/MS-based shotgun lipidomics. (A) CER[NDS], (B) CER[NS], (C) CER[NP], (D) CER[NH]. Data are presented as means ± S.D., $n = 3$.

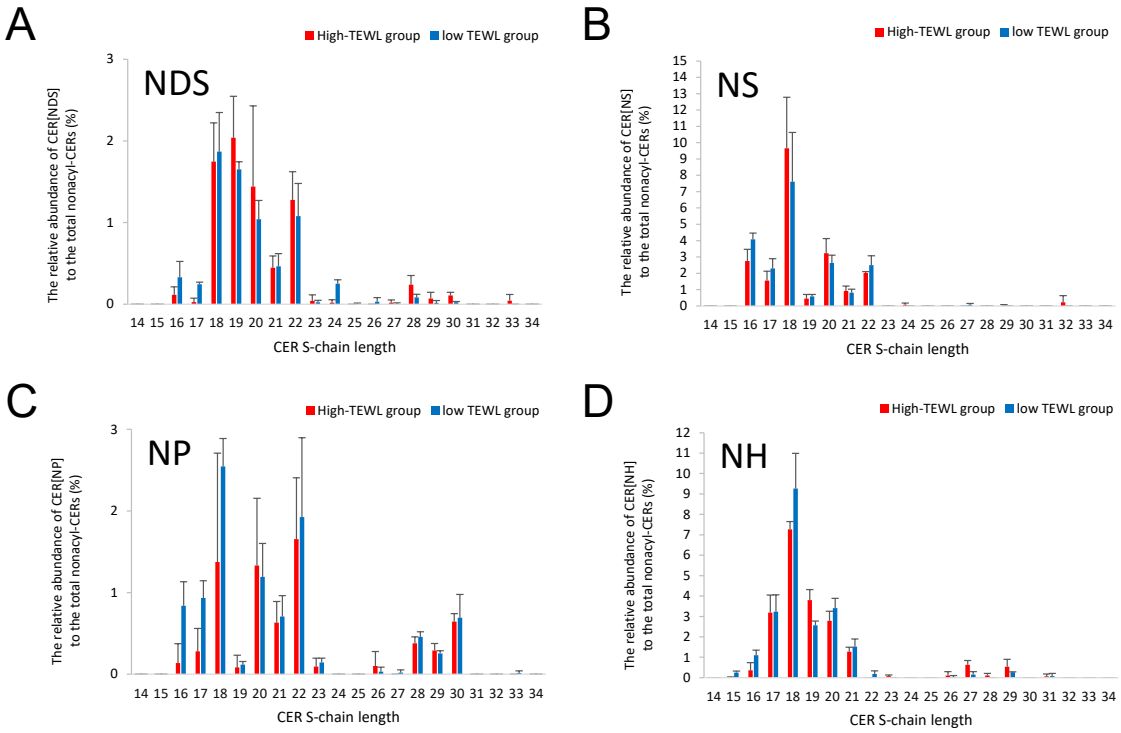

Fig. 15. Proportions of Sphingoid Bases According to S-Chain Length in CER Subclasses Containing alpha-Hydroxy Groups

The relative abundance of each CER to the total nonacyl-CERs (%) was quantified by ESI/MS/MS-based shotgun lipidomics. (A) CER[NDS], (B) CER[NS], (C) CER[NP], (D) CER[NH]. Data are presented as means ± S.D., $n = 3$.

4. Discussion

This study is first to visualize the distribution of the domains formed by packing structure of intercellular lipids in SC cell units using FPA-based FTIR imaging, and it confirmed that the proportions of OR, OR/HEX, HEX/LIQ, and LIQ differed between the high- and low-TEWL groups. This measurement method accurately captured the phase transition behavior of *n*-tricosane, and the phase transition temperatures shown in Fig. S2 were estimated to be about 41 °C for orthorhombic-FCO and about 48 °C for hexagonal-liquid crystal, consistent with previously reported values.[83,94–96)]

Conventionally, X-ray diffraction measurements have been used to evaluate the packing structure in terms of the hexagonal/orthorhombic ratio ($R_{\mathrm{Hexa/Orth}}$).[17,55,102)] However, intercellular lipids contain not only orthorhombic and hexagonal packing structures, but also liquid crystals.[9,83)] Our FPA-based FTIR imaging could determine the LIQ proportion.

The FPA-based FTIR imaging method used in this study is based on more than 4,000 spectra of 64 x 64 FPA elements. Furthermore, by collecting samples in SC cell units by grid stripping, it was possible to evaluate the distribution of domains formed by intercellular lipid packing structures in SC monolayers, which are easily penetrated by IR and are aligned horizontally. Our results revealed that the high-TEWL group had a significantly decreased OR proportion. The proportions of HEX/LIQ and LIQ tended to be higher in the high-TEWL group. The domain size of the packing structure has been determined using electron diffraction measurements.[10)] Our method made it possible to visualize the planar distribution of domains formed by packing structures consisting of a heterogeneous mixture of OR, OR/HEX, HEX/LIQ, and LIQ. No consistent trend was observed in the sizes of these domains. There was a heterogeneous planar distribution of domains formed by packing structures, suggesting the existence of defects in the barrier of the microdomain.

I revealed that the proportion of OR was lower in the domains formed by packing structure distribution near the surface of the SC in skin with high TEWL, and that this decreased proportion affected barrier function.

The reason for the decreased OR proportion in the high-TEWL group was evaluated in terms of the ratio of each CER class to the total nonacyl-CERs and the ratios of FAs or sphingoid bases by chain length for each alpha-hydroxyceramide subclass to the total nonacyl-CERs. The ratio of each CER class to the total nonacyl-CERs in this study (Fig. 11) was consistent with those in earlier studies.[29,100] A high correlation has been reported between TEWL and the relative abundance of CER[AS].[11] I revealed that not only CER[AS] but also the proportion of CER[AP] was increased in the high-TEWL group (Fig. 11). By contrast, a decrease in CER[NP] was observed in high-TEWL skin (Fig. 11), consistent with previous reports showing a negative correlation between TEWL and the relative abundance of CER[NP].[11] The characteristics of the distribution of FA chain lengths in alpha-hydroxyceramides (CER[AS], CER[AP] and CER[AH]) were consistent with those of a study by Kawana *et al*.[90] The change in the distribution of FA chain lengths in CER[ADS], CER[AP], and CER[AS] (Table 4) suggests that alpha-hydroxyceramide influences the domains formed by packing structure proportion. Similarly, the differences in the distribution of C- and S-chain lengths in CER[NP] (Table 4) suggests that these differences affect the proportion of each phase. Figure 14 shows that the C-chain length distribution of CER[NP] shows a characteristic decrease in the long C24 and C26 hydrocarbon chains in the high-TEWL group, which is thought to be one of the factors reducing hydrophobic interactions and thus lowering barrier function. The S-chain length distribution of CER[NP], shown in Figure 15, indicates that there are more C16, C17, and C18 hydrocarbon chains with short hydroxyl groups in the high-TEWL group, which also reduces hydrophobic interactions and can impair barrier function.

In particular, the present study showed that alpha-hydroxyceramides with abundant C24 and C26 elongated FA chains in the C-chain were increased in the high-TEWL group (Fig. 12). I previously reported that the combination of short-chain CER[ADS]-C18/16 (sum of carbon atoms in LCB/FA) and short-chain free FAs results in a packing structure with low barrier function.[103,104] This is thought to be due to the reduced hydrophobic interaction between CER[ADS] and short-chain free FAs.[103,104] Short-chain free FAs were increased in SCs from atopic eczema patients[31], and it is assumed that short-chain free FAs are similarly increased in high-TEWL skin. Therefore, the high proportions of C24 and C26 FA chains in the CER[AS] and CER[AP] alpha-hydroxyceramide subclasses are prone to weaken the packing structure by reducing hydrophobic interactions. The results are also consistent with a study of lipid model membranes, which reported that alpha-hydroxylation of CERs (CER[AS] and CER[AP]) decreased resistance to water loss.[41] On the other hand, the finding that the distribution of S-chain lengths in CER[ADS] and CER[AP] differed between the high- and low-TEWL groups (Table 4) suggests that the difference in the distribution of S-chain lengths affects the proportion of domains formed by packing structures. Figure 13 shows that in the chain length distribution of CER[ADS], there was generally a low proportion of long C22 saturated hydrocarbon chains in the high-TEWL group. When the S-chain is dihydrosphingosine, there is no 4,5 trans double bond in the sphingoid base, and free rotation between carbon atoms is not constrained. Furthermore, because there is no additional hydroxyl group at the C4 position, the

interfacial area per head group is smaller than that of phytosphingosine CER[52], facilitating the formation of a more tightly packing structure, and the long C22 saturated hydrocarbon chain is thought to contribute to maintaining barrier function. By contrast, Figure 13 shows that in the chain length distribution of CER[AP], there were generally more S-chains with long C22 hydroxyl groups in the high-TEWL group. Compared to sphingosine CER, CER[AP] is characterized by a larger interfacial area per head group and difficulty in forming a densely packing structure[52], and the decrease in hydrophobic interaction due to the difference in alkyl chain lengths between CER and free FAs may contribute to reduced barrier function.

It was suggested that the decreased OR proportion in the high-TEWL group was caused by change in the total CER content of CER[AS], CER[AP]and CER[NP], and by the changes in the distribution of their chain lengths.

The mean subject age was higher in the high-TEWL group than in the low-TEWL group (Tables 3 and S2). Therefore, changes in CER chain length distribution may be influenced by age. Future studies should confirm whether these changes are still observed after excluding the effect of age.

Visualizing the distribution of the domains formed by packing structure and elucidating CER subclass alterations in intercellular lipid constituents will facilitate a detailed understanding of skin barrier function. This visualization technique is different from other visualization methods for the whole face, water content[105], and TEWL.[106] Our method characterizes the distribution of the domains formed by packing structure at the microscopic level, and can obtain images of the lipid molecular structure in a single corneocyte. It is expected to be able to detect changes in the lipid molecular structure after topical application

of cosmetics and pharmaceuticals that demonstrate high transdermal absorption or the ability to improve barrier function.

5. Conclusion

The distribution of the domains formed by packing structure in the SC was analyzed using FPA-based FTIR imaging. This method enabled us to determine the proportions of OR, OR/HEX, HEX/LIQ, and LIQ, which has not previously been achieved with conventional averaged peak positions. I also successfully visualized the distribution of domains formed by packing structures in skin SC, and showed that these structures were heterogeneous. The OR proportion was lower in the SC of the high-TEWL group, and this is thought to be associated with the increased proportion of particular alpha-hydroxyceramides in the SC.

CHAPTER 3

Amino acids and their *n*-acetylated derivatives maintain the skin's barrier function

1. Introduction

The SC plays an inside-out barrier function to inhibit water evaporation from the body and an outside-in barrier function to prevent the entry of external allergens. The barrier function of the SC is regulated mainly by intercellular lipids, which include CERs, CHOL, and FFAs[82]. Intercellular lipids form lamellar structures with different periodicities[8]. The lamellar structures are composed of different hydrocarbon-chain packing structures, including Orth, Hex, and a fluid or liquid crystal state[107]. The lamellar structure of intercellular lipids was influenced by SC water content[108]. The ratio of Orth in the lateral packing has been reported to decrease in the surface layer of the SC[12]. The outflow of constituent lipids due to detergent from the SC surface layer has also been proposed to occur[109]. The barrier function of SC intercellular lipids is routinely exposed to various risks, including dehydration and excessive washing which can cause the failure of SC maturation.

Barrier function has been proposed to be enhanced by a high Orth ratio[12]. Based on the results of our previous study, I hypothesized that increasing the Orth ratio by applying non-toxic agents to defective SC will instantaneously improve barrier function. Some chemical agents were previously determined to be transdermal absorption enhancers that affect the intercellular lipid barrier by promoting fluidity and decreasing the Orth ratio[110–113]. However, agents that can restore the intercellular lipid packing structures directly have thus far not been identified except for CER[85,114–116] and FFA[114], which are known intercellular lipids.

I attempted to identify ingredients that can improve the hydrocarbon-chain packing structure from among known moisturizing ingredients. I focused on natural moisturizing factors (NMF)[117] abundant in the SC. Amino acids are a major class of NMF, and their derivatives are widely used as moisturizing agents. In addition, I previously observed lamellar structures with different periodicities and hydrocarbon-chain packing properties using an intercellular lipid model (*N*-(alpha-hydroxyoctadecanoyl)-dihydrosphingosine (CER[ADS])/Palmitic acid (PA)/CHOL). This difference in lamellar structures are thought to be caused by the difference in whether or not FFA are contained in the membrane[103]. In the lipid bilayer, FFA are subject to mutual control of the Born energy, which desorbs charged carboxyl groups from the lipid bilayer, and the hydrophobic interaction energy, which retains the protonated FFA in the lipid

bilayer[118]. It is assumed that the hydrocarbon-chain packing structure can be improved by controlling the position of FFA in the lamellae with charged substances such as amino acids.

Therefore, the effects of improving the hydrocarbon-chain packing structure of NMF were investigated using those models. *N*-Acetyl-L-hydroxyproline (AHYP), which maintains barrier function[119], is widely used in cosmetics. In this report, I determined the effects of improving the hydrocarbon-chain packing structure of the amino acid derivative acetyl hydroxyproline (AHYP).

In this study, I determined the effects of improving the hydrocarbon-chain packing structure of amino acids by applying to an established intercellular lipid model. The amino acids used in this study were either neutral, acidic, or basic. In order to study their effects on our model, I first performed DSC. DSC is a powerful methodology that can reveal structural changes of lipids in bilayers and lamellae by measuring phase transition enthalpies. The structural changes identified were subsequently analyzed in detail using SAXS and WAXD. Next, for any amino acid that showed significant effects in the intercellular lipid model, I performed structural analysis using time-resolved SAXS and WAXD measurements to determine if similar structural changes are observed in human SC.

2. Experimental

2.1. Chemical reagents

L-Serine (Ser, >99%), L-alanine (Ala, >99%), L-glutamine (Gln, >99%), and L-(+)-arginine (Arg, >99%) were purchased from Tokyo Chemical Industry Co., Ltd. (Tokyo, Japan). L-glysine (Gly, >99%) and glutamic acid (Glu, >99%), were purchased from Kanto Chemical Co., Inc. (Tokyo, Japan). L-hydroxyproline (Hyp, 98.5%), *N*-acetyl-L-hydroxyproline (AHYP, 99%), and *N*-acetyl-L-glutamine (AGLN, 98.5%) were purchased from Kyowa Hakko Bio (Tokyo, Japan). (2*S*,3*R*)-2-(2-hydroxyhexadecanoyl)aminooctadecane-1,3-diol (95%):Ceramide [ADS]-C18/16 (CER[ADS]) was generously supplied by Takasago International (Tokyo, Japan). Palmitic acid (PA, ≥99%) and cholesterol (CHOL, ≥99%) were purchased from Sigma-Aldrich (St. Louis, MO, U.S.A.). Methanol and chloroform used were of reagent grade. All other chemicals used were reagent grade.

2.2. Preparation of lipid model

A lipid model containing CER[ADS], PA, and CHOL (CER[ADS]:PA:CHOL, 26.5:59.6:13.9, %mol) was prepared as previously reported[61,103]. Since the Orth ratio of this lipid model resembled that of human SC[17], I did not alter its lipid composition ratio. The lipid model was therefore prepared as follows. The lipid mixture was dissolved in methanol: chloroform (1:2, v/v) in an eggplant-shaped flask. The solvent was removed by a rotary evaporator *in vacuo* for 24 h. The thin lipid film was hydrated for 30 min above the phase transition temperature (~85°C) using acetate buffer (pH 5.3). After the film was removed from the flask, it was subjected to ultrasonic irradiation (VCX 130 PB, Sonics & Materials, Inc., Newtown, CT, U.S.A.) for 5 min above the phase transition temperature (approx. 85°C). The total lipid concentration was adjusted to 10 mM using acetate buffer. In addition, amino acids were added to the bilayer suspension, and their total concentration was adjusted to 0.1 M at room temperature. Due its low solubility, Glu was used at saturated concentration i.e. 57 mM. The CER[ADS]/PA/CHOL bilayer suspension was stored overnight at room temperature. Vesicle aggregates were suction-filtered and dried, and used as the intercellular lipid model for our experiments.

2.3. DSC measurements

DSC measurements were carried out using a DSC-7020 (Hitachi High-Tech Co., Tokyo, Japan), over temperatures ranging from 20–120°C with heating scans at a rate of 2.5°C/min. Lipid models weighing approximately 6–12 mg were placed in aluminum pans with covers (Seiko Instruments Co., Chiba, Japan).

2.4. Preparation of human SC sheets

Human abdominal SC sheets were purchased from Biopredic International (Saint-Grégoire, France). The procedure to separate SC sheets from human skin was as follows. Skin was floated on 0.25% (w/v) trypsin dissolved in phosphate-buffered saline (PBS), pH 7.4, at 30°C for 4 h. Thereafter, the SC was separated from the skin. Prepared SC sheets were rinsed three times in distilled water. Either 20% AHYP (w/w) or water as a control was applied to the dried SC.

2.5. SAXS and WAXD measurements

SAXS and WAXD profiles of our intercellular lipid model were obtained using BL40B2 located at the SPring-8 (Hyogo, Japan). Sample-to-detector distance and the X-ray wavelength were approximately 540 mm and 0.083 nm, respectively. The energy of the X-rays was 15 keV. X-ray scattering and diffraction data were collected using an R-Axis VII imaging plate detector (Rigaku, Tokyo, Japan); exposure time was 30 s. Sample temperature was maintained at 32°C using an FP-99 DSC (Mettler-Toledo, Tokyo, Japan). A sample cell containing intercellular lipid model was sealed with polyimide film (Kapton EN, Du Pont-Toray Co., Ltd., Tokyo, Japan) and placed in the X-ray diffractometer's sample holder.

2.6. Time-resolved SAXS and WAXD

Time-resolved SAXS profiles of human SC sheets were obtained using the BL40B2 located at the SPring-8. Measurement conditions were the same as for our intercellular lipid model. An approximately 5 mg of the SC was placed in a 1-mm capillary glass tube. Immediately after the sample solution was applied to the SC, X-ray exposed for 60 s and repeated at 120 s intervals up to 60 min after application at 32°C.

WAXD profiles of human SC sheets were obtained using BL19B2 located at the SPring-8. Sample-to-detector distance and the X-ray wavelength were approximately 769 mm and 0.049 nm, respectively. The energy of the X-ray was 25 keV. X-ray diffraction data were

collected using PILATUS 2M semiconducting detector (Dectris Ltd., Baden-Daettwil, Switzerland). Sample temperature was maintained at 32°C using an FP-99 DSC. For WAXD measurement, approximately 0.2 mg SC were stacked and set at the edge of a 1 mm capillary glass tube so that X-rays were emitted perpendicularly to the glass tube. Each sample was exposed for 30 s at 150 s intervals up to 15 min after sample solution application. Diffraction intensity was standardized by the incident X-ray intensity in front of the sample.

The scattering and diffraction intensities I were plotted as a function of the scattering vector q, defined as $q = (4\pi\sin\theta)/\lambda$, where θ is the scattering angle and λ is the wavelength. The periodicity of the lamellar phases d from the positions of series of equidistant peaks (q_n) using the equation $d = 2n\pi/q_n$, where n is the order number of the scattering peak. Spatial calibration was performed using silver behenate. The circular average of the scattering and diffraction patterns was calculated to obtain a radial intensity profile.

2.7. Data analysis

The resulting SAXS and WAXD profiles were analyzed using the software Origin (Light Stone Co., Tokyo, Japan) to determine the integrated intensity, peak position, and full width at half maximum (FWHM). SAXS profiles were fitted using the Lorentzian function and WAXD profiles were fitted using a Gaussian function. The increase in FWHM indicates disturbance of the lamellar structure. Due to weakening of the interference effect, the scattering peak becomes a broad peak.

The resulting DSC thermograms were analyzed using the software Origin (Light Stone Co., Tokyo, Japan) to determine the transition enthalpy and phase transition temperature. DSC thermograms were fitted using a Gaussian function. Transition temperatures were determined as the maxima of the endothermic transition peaks.

Lorentzian function : $y = y_0 + \frac{2A}{\pi} \cdot \frac{w}{4(x-x_0)^2+w^2}$

Gaussian function : $y = y_0 + \frac{A}{w\sqrt{\frac{\pi}{4\ln(2)}}} \cdot \exp\frac{-4\ln(2)(x-x_0)^2}{w^2}$

Here, y_0 is the offset for baseline correction; the peak area is represented by A, w is the full width at its half maximum, and the center of the peak is denoted as x_0.

3. Results

3.1. Effect of amino acids on the nanostructure of CER[ADS]/PA/CHOL bilayers

I previously reported that the intercellular lipid model (CER [ADS] / PA / CHOL) used in this study contains two phases with different lamellar periodicities. I found that Phase A has a 4.6 nm periodicity lamellar structure with Orth and Hex packing. In contrast, Phase B has a 4.3 nm periodicity lamellar structure with packing structure different from that of Orth and Hex. The hydrocarbon-chain packing structure of Phase B also has a lower proportion of Orth relative to Phase A. Therefore, I concluded that Phase B has a weak barrier function.

Figure 16(a) shows a lipid model thermogram while Fig. 16(b) shows the change in normalized integrated intensity of each lamellar phase as a function of temperature. The original thermogram of our lipid model is shown in black while Phase A-derived, Phase B-derived, and mainly PA-derived fitted curves are shown in green. The phase transition temperature of the endothermic peak observed by DSC and the temperature range and FWHM of the scattering

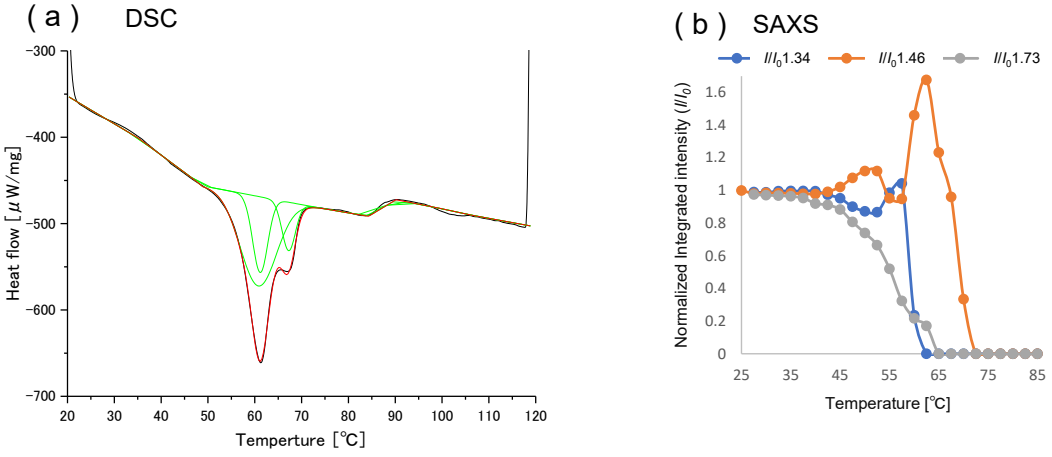

Fig. 16. Three Phases with Different Thermal Characteristics in a Lipid Model

DSC thermograph and SAXS profiles of the CER[ADS]/PA/CHOL lamellae lipid model used in our study. (a) DSC thermograph of the lipid model. Three endothermic peaks generated by performing curve fitting based on the Gaussian distribution are shown as green lines. The cumulative fitting curve is shown as a red line. (b) Overlay plot of the change in normalized integrated intensity of each lamellar phase, namely Phase A, Phase B, and PA Phase as a function of temperature (25–85 °C). (Color figure can be accessed in the online version.)

intensity of the lamellar structure observed by SAXS are summarized in Table 5. Based on their

thermotropic behavior, endothermic peaks were classified as either PA-derived, Phase A-derived, and Phase B-derived in the order of the lower phase transition starting temperatures. The characteristic of lamellar structures with different periodicities determined by SAXS can be attributed to DSC measurements.

Amino acids were applied and evaluated during preparation of the intercellular lipid

Table 5. Phase Transition Temperatures and FWHM of Phase A, Phase B, and PA Phase Are Summarized

Measurement method	Phase A		Phase B		PA phase	
	T (°C)	FWHM	*T* (°C)	FWHM	*T* (°C)	FWHM
DSC	61.16	3.78	67.24	3.36	60.76	9.10
SAXS	60–62.5	0.12	65–72.5	0.14	45–62.5	0.06

model. Table 6 summarized the transition enthalpies, phase transition temperatures, and FWHM of individual amino acids that were applied. Neutral amino acids, namely Ser, Ala, Hyp, and Gln, caused a large change in both Phase A and Phase B in terms of transition enthalpy, phase transition temperature, and FWHM. In contrast, a group of acidic amino acids comprising AHYP, AGLN, and Glu caused FWHM to increase, as well as both the phase transition temperature bands, Phase A and Phase B. Those compounds possess a negative charge on either their side chain or their alpha-carboxyl group. A basic amino acid, Arg, reduced the transition enthalpy in Phase A.

The thermogram that I obtained following AHYP application was shown in Fig. 17.

Table 6. Sample Categories and DSC Measurement Parameters for Each Lamellar Phase

Sample	Categories	Phase A			Phase B			Total enthalpy change ΣΔH (μJ/mg)
		Δ*H* (μJ/mg)	*T* (°C)	FWHM	Δ*H* (μJ/mg)	*T* (°C)	FWHM	
Control	—	352.50	61.16	3.78	200.85	67.24	3.36	553.35
Ser	Neutral	278.00	63.80	3.80	151.88	69.79	3.40	429.88
Ala		380.27	63.16	3.89	164.26	68.75	3.41	544.52
Gly		159.95	63.62	4.62	156.88	70.29	3.82	316.83
Hyp		375.95	64.65	3.83	277.32	69.12	3.46	653.27
Gln		362.89	65.00	5.25	245.43	69.73	3.16	608.31
AHYP	Acidic	305.95	65.88	12.00	258.54	74.61	4.74	564.49
AGLN		361.12	67.10	12.39	289.51	74.49	4.97	650.63
Glu		275.90	65.56	9.77	370.99	73.16	5.27	646.88
Arg	Basic	109.64	62.94	2.90	266.53	69.59	3.56	376.16

The phase transition temperature of Phase A was 65.9°C, higher than that of the control (61.2°C). Similarly, the phase transition temperature of Phase B was 74.6°C, higher than that of the

control (67.2°C). In contrast, the phase transition temperature zone corresponding to phase-separated PAs decreased to between 40–55°C.

Since the amino acid derivative AHYP maintains barrier function[121], it is widely used in formulating cosmetics. I therefore decided to conduct a more detailed study focused on AHYP.

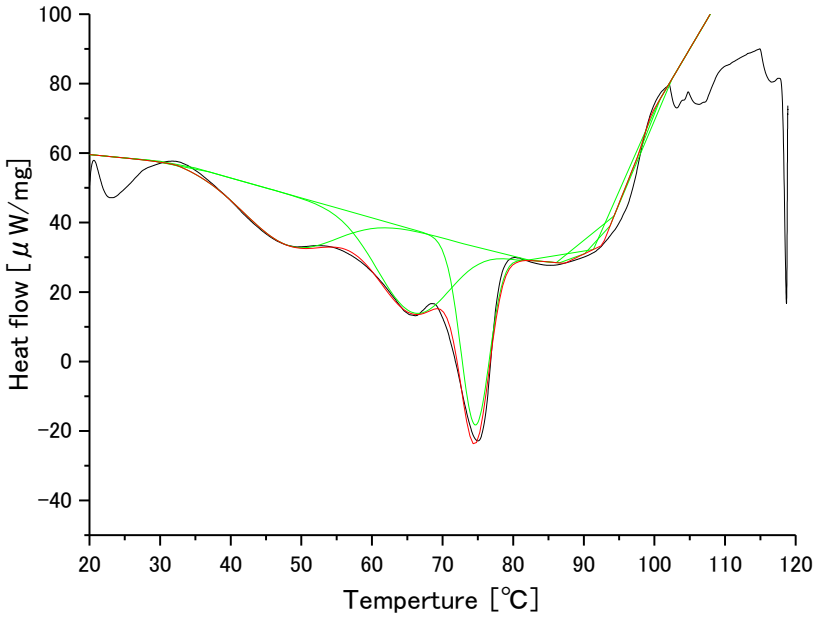

Fig. 17. Thermograph of Lipid Model with AHYP Applied

Three endothermic peaks generated by performing curve fitting based on the Gaussian distribution are shown as green lines. The cumulative fitting curve is shown as a red line.

3.2. Effect of AHYP on the nanostructure of CER[ADS]/PA/CHOL bilayers

I focused on AHYP, which had a significant effect on the intercellular lipid model CER[ADS]/ PA/CHOL, using SAXS measurements. SAXS measurements are useful for analyzing lamellar structures and determining the lamellar period of lipid membranes. Figures 18(a) and 18(b) showed the scatter profiles of lipid model at 25°C for application of AHYP and control. Scattering peaks observed at approximately $q1 \approx 1.3$, $q2 \approx 2.7$, and $q3 \approx 4.1$ nm^{-1} were derived from lamellar structures with a lamellar period of 4.6 nm, and the scattering patterns indicate the presence of a Phase A of short-period lamellar structures. Scatter peaks from other

structures were also observed in the vicinity of scatter peaks from Phase A. This distinct scatter peak was observed at approximately $q1 \approx 1.4$, $q2 \approx 3.0$, and $q3 \approx 4.5$ nm^{-1}, with a lamellar period

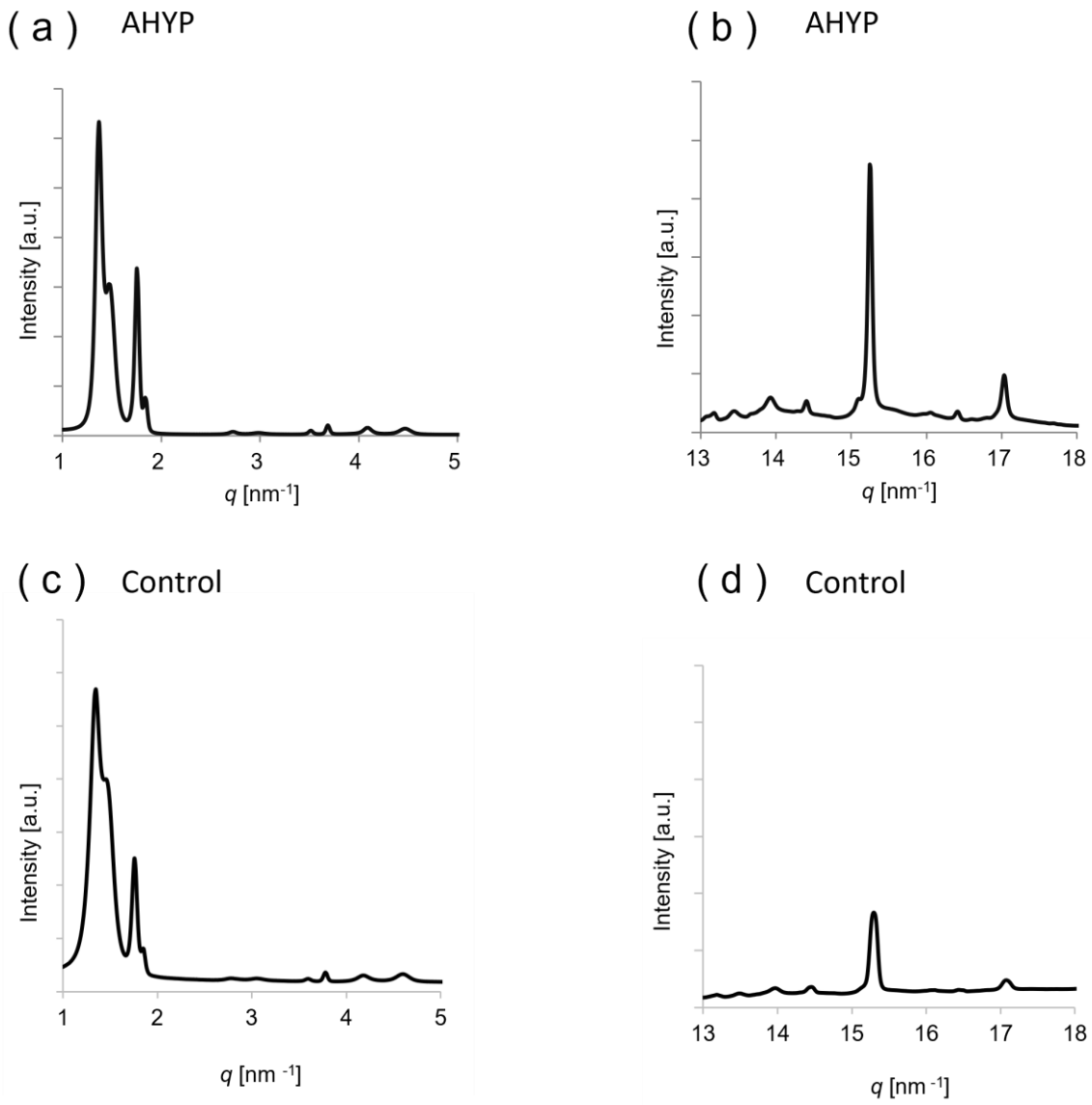

Fig. 18. SAXS and WAXD Profiles of CER[ADS]/PA/CHOL Lamellae at 25 °C

SAXS (left row) and WAXD profiles (right row) of a lipid model following AHYP application (a and b, respectively) are

of 4.3 nm derived from the lamellar structure, indicating the presence of Phase B in the short-period lamellar structure.

The peak positions, peak intensities, and FWHM of Phases A and B are summarized in Table 7. In the AHYP-applied model, the FWHM of Phase A was reduced to 0.075 compared with 0.122 for the control. Similarly, FWHM of Phase B was reduced to 0.119 compared to 0.138 for the control. In addition, I observed no change in the ratio of Phase B/Phase A in the integrated intensity comparison and not intensity comparison, but this ratio decreased to 0.36 following AHYP application compared with 0.51 for that of the control. SAXS analysis, which complemented the DSC measurement, showed a decrease in the intensity of Phase B relative to Phase A (Table 7). Additionally, AHYP application decreased Phase B. Next, I investigated the effect of AHYP on human SC by measuring SAXS and WAXD simultaneously.

Table 7. Peak Position, Peak Intensity, FWHM, and Peak Intensity Ratio Determined by Simultaneous SAXS and WAXD Measurements

	Phase A (25 °C)		FWHM	Phase B (25 °C)		FWHM	Ph B/Ph A peak ratio* (25 °C)
	Peak position (nm^{-1})	Peak intensity (a.u.)		Peak position (nm^{-1})	Peak intensity (a.u.)		
Control	1.345	10289	0.122	1.474	5214	0.138	0.51
AHYP	1.371	63028	0.075	1.486	22530	0.119	0.36

* The abbreviations PhA and PhB correspond to Phase A and Phase B, respectively.

3.3. Effect of AHYP on the human SC determined by SAXS

Either AHYP or water, as a control, was applied to SC at 25°C and changes were determined by time-resolved SAXS. The result revealed the changes in lamellar structure as shown in Figs. 19(a) and 19(b). The scatter peaks observed at approximately $q1 \approx 0.97$, $q2 \approx 1.85$, and $q3 \approx 2.80$ nm^{-1} were from short-period lamellar structures with a period of 6.4 nm. Scattering peaks from other structures were also observed in the vicinity of peaks from short-period lamellar structures. This distinct scatter peak was observed at approximately $q1 \approx 0.44$ and $q3 \approx 1.33$ nm^{-1}, and the lamellar period was derived from a lamellar structure of 14.2 nm, indicating the presence of a long-period lamellar structure.

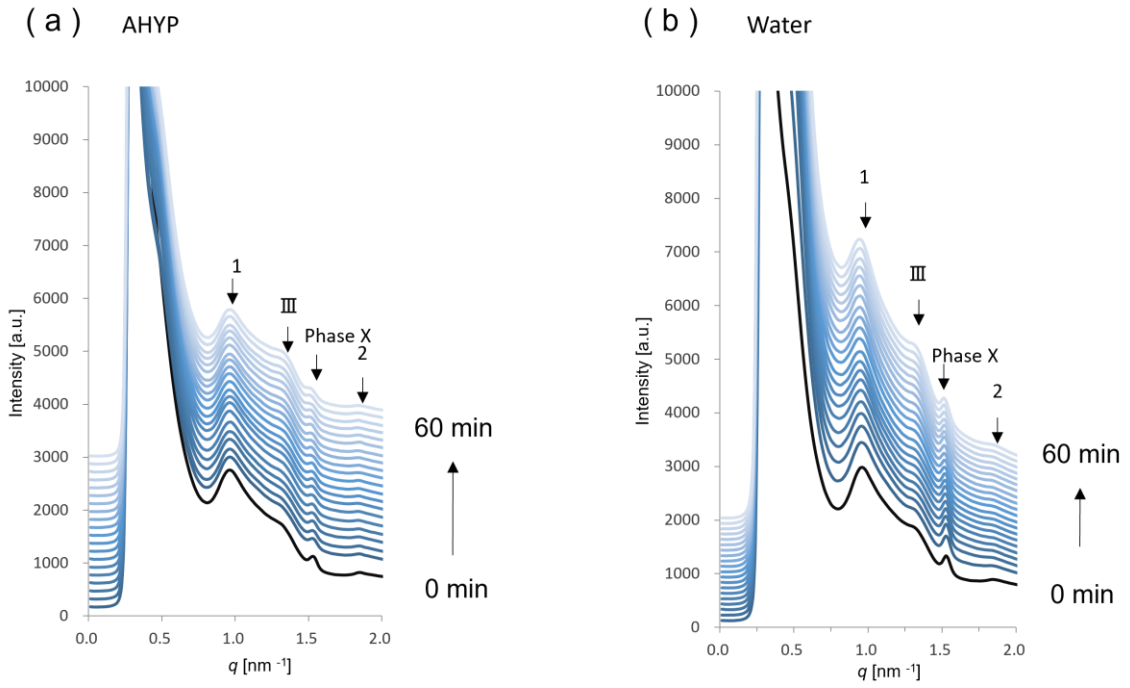

Fig. 19. SAXS Profile of Phase X

SAXS profiles collected from the CER[ADS]/PA/CHOL lamellae used in our study are shown. Note the changes in X-ray scattering peak intensities of the lipid model following application of either AHYP or water. SAXS intensity profiles collected from 0 to 60 min are indicated by a change in intensity from dark to light blue (black line: 0 min) (a) SAXS profiles with AHYP applied. (b) SAXS profiles of a control lipid model. Roman numerals (III) indicate the scattering 3rd order of the LPP. Arabic numerals indicate the different scattering orders of the SPP.

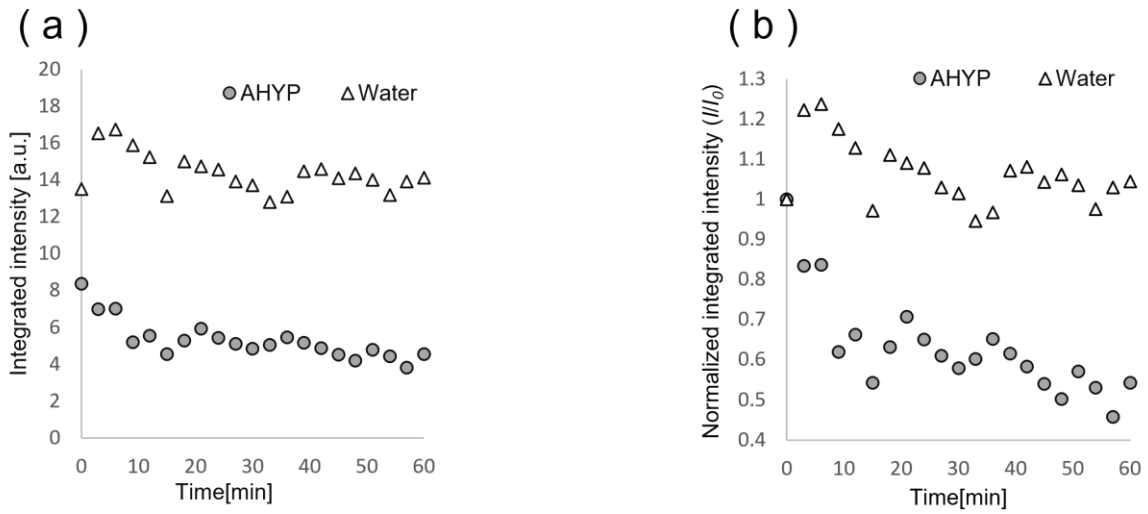

Fig. 20. SAXS Profiles Collected from 0 to 60 min after Application of Either AHYP or Water

(a) Parameters for integrated intensity where scattering peak was observed at approximately $q \approx 1.53$ from Phase X. (b) Overlay plot of the change in normalized integrated intensity from Phase X of each application sample.

Those lamellar structures showed values close to those previously reported for the short periodicity phase (SPP) in SC, but they were slightly longer than the 13.4 nm lamellar period reported for the long periodicity phase (LPP) in SC.[8] No significant changes in SPP and LPP were observed when AHYP and water were applied. However, I observed a different lamellar structure (Phase X) with a lamellar period of 4.1 nm, whose scattering peaks were observed at approximately $q1 \approx 1.53$, $q2 \approx 3.06$, and $q3 \approx 4.59$ nm^{-1}. I considered the phase transition temperature of Phase X to be around 65°C (Fig. S4), and it had the same thermal property as the phase transition of Phase B at around 65°C in the intercellular lipid model.[105] Since the peak position of Phase X differs depending on individual differences in the SC,[122] the peak position $q1 \approx 1.47$ (Fig. S4) that I observed in this study is thought to be derived from Phase X. This idea is consistent with the peak position $q1 \approx 1.474$ (Table 7) for Phase B. Based on these observations, I believe that Phase X correspond to Phase B in the intercellular lipid model. I therefore focused on this Phase X. Figure 20 showed the consequences of the integrated intensity due to the change in Phase X. When water was applied, the integrated intensity from Phase X was temporarily increased. However, the scattering intensity of Phase

X did not change between before and 60 min after applying water. When AHYP was applied, however, I verified that the scattering intensity derived from Phase X decreases by half over time. Figure 20(b) showed the results of comparing the integrated intensity change (Fig. 20(a)) as I/I_0. Even when the initial values were uniform, the scattering integrated intensity derived from Phase X decreased following AHYP application.

3.4. Effect of AHYP on human SC determined by WAXD

I determined AHYP's effects on the hydrocarbon-chain packing structure, which significantly altered the CER[ADS]/PA/CHOL ratio of intercellular lipid model, was determined by WAXD. Supplemental Figure S4 shows the WAXD profiles of AHYP and water applied to human SC at 25°C. Figure 21 shows the consequences of the change in the integrated intensity derived from Hex (I_{Hex}) and Orth (I_{17}). I_{Hex} was calculated from the integrated intensity of diffraction peaks observed around $q \approx 15$ nm^{-1} (P_{15}) and $q \approx 17$ nm^{-1} (P_{17}). I_{17} was calculated from the integrated intensity of P_{17}. These results are consistent with the sample data from human SC with AHYP measured by WAXD profiles (Fig. S5).

I verified that I_{17} derived from Orth increased 9 min after the start of dehydration, but returned to the same integrated intensity as before application 15 min after the start of dehydration. When water was applied, however, the I_{17} decreased with dehydration after application. After 15 min of dehydration, the intensity was decreased, as was the Orth ratio. Therefore, I propose that the application of water disrupted the hydrocarbon-chain packing structure of intercellular lipids during the dehydration process.

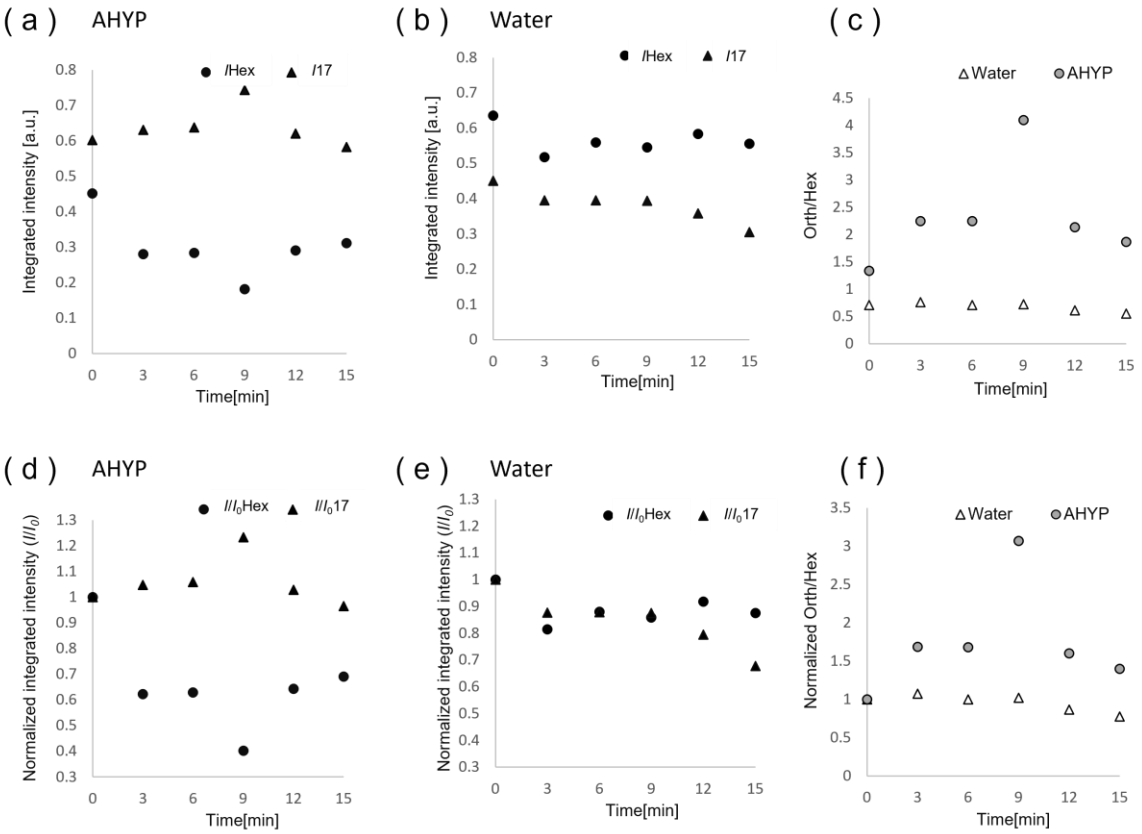

Fig. 21. WAXD Profiles Collected from 0 to 15 min after the Application of Either AHYP or Water

(a) Parameters for integrated intensity where scattering peaks were observed at approximately $q \approx 15$ nm^{-1} from Hex ((I_{Hex} : I_{15}−2 ×I_{17})/3) and $q \approx 17$ nm^{-1} from Orth (I_{17}) with either AHYP applied or (b) water as control. (c) Overlay plot of the change in I_{17}/I_{Hex} ratio. (d) Normalized integrated intensity from data shown in (a). (e) Normalized integrated intensity from data of (b). (f) Normalized I_{17}/I_{Hex} ratio from data shown in (c).

Discussion

In this study, I found that AHYP maintains lipid packing structure by using intercellular lipid model, and verified its effects on human SC. I propose that AHYP altered the intercellular lipid packing structure by electrostatic interactions. I also propose that applying AHYP to the intercellular lipid model increased the phase transition temperature of Phase A and improved the membrane's thermal stability. I had proposed two possible mechanisms: either the lipid composition of Phases A and B has changed, or that AHYP application changed the lipid configuration.

Bouwstra *et al*. previously reported that cholesterol sulfate reduces the ratio of lamellar phases with similar lamellar period to that of Phase B in their intercellular lipid model. They reported that the sulfonic acid group of dissociated cholesterol sulfate increases the interface area per lipid molecule and decreases the packing density, thereby increasing the solubility of CHOL.[67] In our study, I inferred that AHYP did not enhance CHOL solubility based on the absence of observed reduction in phase-separated CHOL in Fig. 18(a). I assumed that the carboxylic groups of acidic amino acids act as negative charge donors in our intercellular lipid model. This idea was supported by not only the increase in phase transition temperature for Phases A and B, but also the increase in FWHM of both phases. In our previous study, I considered Phase A as being composed of CER, CHOL, and PA, whereas Phase B was composed of only CER and CHOL.[103] Moore *et al*. determined that in the PA-based domain, the phase transition temperature range of perdeuterated PA in their intercellular lipid model was 42.5–62°C,[121] which agrees with the phase transition temperature range derived from the scatter peak at $q \approx 1.73$ nm^{-1}. I concluded that this scattering peak was derived from the crystalline phase composed mainly of PA (i.e. the PA Phase). The carboxylic groups of acidic amino acids were negatively charged in acetate buffer with a pH of about 5.3. I thought that the negative charges of these acidic amino acids suppressed PA elimination from Phase A due to electrostatic repulsion.[122] I hypothesized that maintaining PAs within Phase A leads to local lipid composition changes and increases the phase transition temperature; however, suppressing PA elimination also leads to non-uniformity in the hydrocarbon-chain packing structure, resulting in increased FWHM.

I observed that acidic amino acids elevate the phase transition temperature and FWHM, especially in *N*-acetylated amino acids, AHYP and AGLN (Table 6), whose amino groups were protected by the acetyl group. I hypothesized that the electrostatic interaction between negatively charged acidic amino acids and dissociated PA suppresses PA elimination from Phase A. In contrast, the positively charged amino acid, Arg, reduced not only the transition enthalpy but also Phase A (Table 6). I assumed that electrostatic attraction between positively charged Arg and negatively charged PA promotes PA withdrawal from Phase A.

Amino acids without charged side chains, namely Ala, Hyp, and Gln, did not cause major changes in either Phase A, Phase B, or the phase transition temperature of FWHM. Those absence of major changes was probably due to the absence of electrostatic repulsion against PA. In contrast, Gly was observed to have a decreased transition enthalpy in both Phases A and B. Most amino acid NMFs have uncharged side chains.[123] The observed decrease in enthalpy may be caused by stereological affinity with Gly. Since acidic amino acids were less abundant than other major amino acids among NMF[123] in the SC, the effects that acidic amino acids exert must be distinguished from the moisturizing effect of NMF.[124] Lamellar conformation may also be maintained by highly dissociative lipids such as cholesterol sulfate.[67,125]

In this study, I determined that AHYP exerted a prominent effect using an established intercellular lipid model. AHYP application to human SC halved the integrated intensity of Phase X (Fig. 19), which was considered a hydrocarbon-chain packing structure with low barrier function.[103] In contrast, the integrated intensity of Phase X was temporarily increased by applying water, although it eventually returned to its original condition (Fig. 20). Similar changes in water content were reported in the short periodicity phase.[108,126] AHYP application increased the Orth ratio, suggesting that the ordered hydrocarbon-chain packing structure was maintained. Based on those data, I proposed that AHYP improves barrier function by reducing Phase X in human SC.

Considering the mechanism of Phase X change in human SC, AHYP inhibits Phase B formation in the intercellular lipid model used in this study. Inhibiting CER conformation changes was thought to increase the order within the hydrocarbon-chain packing structure due to the elimination of FFAs.

At pH 5.3, about 25% of FFA in human SC is dissociated[122] based on the Henderson-Hasselbalch equation.[127] Making the pH of the superficial layer of the SC more acidic should therefore suppress FFA dissociation. The pH deep inside the SC is believed to be approximately 7.4,[67] and that is where FFAs are thought to be more than 90% dissociated[125,127] from intercellular lipids, which suggests that Phase X was more likely to occur. Since the pH of deep inside the SC is difficult to control, delivery of electrostatically interacting agents that can inhibit FFA dissociation is the key factor to reducing Phase X. Small molecules such as AHYP and acidic amino acids are ideal for those purpose.

To date, moisturizing agents are thought to exert their effects based on hydration, occlusion, and physiological effects. No agents are known to maintain barrier function by physicochemical action on intercellular lipids. In this study, I verified that the proportion of intercellular lipids in human SC is decreased by applying water. This finding suggested that SC barrier function may be impaired even by washing one's face without cleaning agents. AHYP application was proposed to maintain the ordered hydrocarbon-chain packing structure of intercellular lipids, and the Orth ratio. AHYP, an *N*-acetylated acidic amino acid, was previously proposed as a useful agent that maintains the barrier function of intercellular lipid by physicochemical action.

Narangifard reported that the lamellar structure and lipid arrangement of intercellular lipids change during human SC maturation.[128] This report suggested that the intercellular lipid hydrocarbon-chain packing structure is not rigid but is, instead, plastic. It also proposed that the efflux of lipids by the lavage agent also occurs in plastically intercellular lipids. Lipid efflux might be appeared to depend on lipid solubility, and the order of lipid elution from intercellular lipids is FFA, CHOL, and CER.[111] Short-chain FFAs have been found to influence the formation of hydrocarbon-chain packing structures[129] and the homogeneity of lipid membranes.[44] The proportion of PA has been reported to increase in cases of atopic eczema.[31] Because of the nature of PA and short-chain FFA, the intermolecular forces between the hydrophobic chains are thought to be weak,[118] PA's solubility is relatively high compared to other intercellular lipids. Thus, PA is easily withdrawn from intercellular lipid bilayers.

Taking advantage of the fact that electrostatic repulsion from amino acids inhibits the

withdrawal of short-chain FFA from the lipid bilayer was valuable for improving the barrier function of pathological skin, which contains a higher proportion of short-chain FFA.[31] This approach was also expected to contribute to preventing the formation of rough skin due to excessive washing during the current (COVID-19) pandemic. I believe that this approach may provide an important avenue for developing new skincare products.

5. Conclusion

In this study, I used an intercellular lipid model consisting of CER[ADS]/PA/CHOL with coexisting lamellar structures of different periodicities to determine the effects of AHYP and acidic amino acids using DSC measurements. I found that AHYP maintains the reduction in Phase X and Orth ratio. I also found that AHYP and acidic amino acids are useful agents for maintaining the hydrocarbon-chain packing structure of intercellular lipids through electrostatic repulsion. In the future, I will expand the scope of this study, which may eventually lead to the development of skincare products that can maintain the skin's barrier function.

Summary

Intercellular lipids in the stratum corneum (SC) protect the living body from invasion by allergens and pathogens, and also suppresses water evaporation within the body. The hydrocarbon-chain packing structure of intercellular lipids in the SC is critical to the skin's barrier function. This packing structure consists of a mixture of crystals (orthorhombic and hexagonal) and liquid crystals (fluid phase), and the proportion of these phases is thought to affect barrier function. However, it is not well understood why these differences in packing structure occur. The details of how the domain distribution of these packing structures exists in the human SC are also unknown. There have been no methods to visualize the actual distribution of the domains formed by packing structure in intercellular lipids.

If I can elucidate the causes of these differences in the packing structure and understand the characteristics of the packing structure in skin with impaired barrier function, I can establish guidelines for normalizing barrier function in the human SC and for developing new barrier function-improving agents.

In Chapter 1, in order to confirm the influence of lipid composition in intercellular lipids, which are composed of a wide variety of lipid species, structural analysis studies have been conducted using models of intercellular lipids with different lipid compositions. I prepared collapsed skin intercellular lipid models constituted short-chain free fatty acid and ceramide which having an alpha-hydroxy group. To investigate the characteristics of the packing structure, the intercellular lipid model (CER[ADS]/CHOL/PA) were adjusted for models with different lipid compositions. The characteristics of the packed and lamellar structures have been determined by temperature-scanning small-angle X-ray scattering and wide-angle X-ray diffraction measurements simultaneously. Studies using intercellular lipid models (CER[ADS]/CHOL/PA) have reported the formation of two phases with different short lamellar periodicities. These differences in lamellar structure were thought to be caused by differences in ceramides (CER) conformation between the hairpin and the V-shape type. The lamellar structure of the V-shaped CER conformation has a low orthorhombic ratio. The above results suggest that an increase in the ratio of CER with the V-shaped structure causes the lamellar structure to have low orthorhombic ratio, thereby contributing to a decrease in the bilayer's

barrier function.

In Chapter 2, the planar distribution of intercellular lipid structures was determined using focal plane array (FPA)-based Fourier transform (FT) IR imaging analysis of SC cell units obtained by grid stripping. The lipid composition of ceramides was revealed by electrospray ionization tandem mass spectrometry (ESI-MS/MS)-based shotgun lipidomics. The distribution of domains formed by packing structures and the lipid composition of ceramides was compared in skin with high- or low-transepidermal water loss (TEWL). The orthorhombic proportion was lower in high-TEWL skin than in low-TEWL skin. ESI-MS/MS-based shotgun lipidomics analysis showed that the alpha-hydroxyceramide content in the low- and high-TEWL groups differed regarding the distribution of fatty acid chain lengths. The evaluation of SC cell units using FPA-based FTIR imaging is an innovative technology that can visualize the distribution of domains formed by intercellular lipid-packing structures. Increased proportions of alpha-hydroxyceramide subclasses such as alpha-hydroxy-sphingosine ceramide and alpha-hydroxy-phytosphingosine ceramide were associated with a reduced proportion of the orthorhombic packing structure domain.

In Chapter 3, I investigated agents that directly increase the Orth ratio. I selected an intercellular lipid model consisting of ceramide, cholesterol, and palmitic acid and performed differential scanning calorimetry. I focused on natural moisturizing factor components in the SC, and therefore investigated amino acids and their derivatives. The results of our intercellular lipid model-based study indicate that *N*-acetyl-L-hydroxyproline (AHYP), remarkably, maintains the lamellar structure. I verified the effect of AHYP on the lamellar structure and hydrocarbon chain packing structure of intercellular lipids using time-resolved X-ray diffraction measurements of human SC. I also determined the direct physicochemical effects of AHYP on the Orth ratio of the hydrocarbon-chain packing structure. Hence, the results of our human SC study suggest that AHYP preserves skin barrier function by maintaining the hydrocarbon-chain packing structure of intercellular lipids via electrostatic repulsion. These findings will facilitate the development of skincare formulation that can maintain the skin's barrier function.

In conclusion, this study clarified one of the factors that reduce the barrier function of

intercellular lipids in the SC by analyzing a simple composition lipid model that mimics the lipid composition of the SC with impaired barrier function through multiple physicochemical evaluations. I also found that the ratio of orthorhombic domains in the packing structure distribution of intercellular lipids is reduced in human SC with impaired barrier function. Based on the mechanism of reduced barrier function, I found the usefulness of *N*-acetylamino acid derivatives as barrier function improvers.

Supplementary datas

Lipid class	Acquisition mode	Precursor ion	Fragment ion	Structural detail	Example	slope/r^2
Non-hydroxy-dehydrosphingosine [NDS]	Neg FTMS/MSMS	$[M+C_2H_3O_2+H.]^-$	$[FA-H^+]^-$	Sub-species	[NDS] 44:0;2 (20:0;2-24:0;0)	nd
Non-hydroxy-sphingosine [NS]	Neg FTMS/MSMS	$[M+C_2H_3O_2+H^-]^-$	$[FA-H^+]^-$	Sub-species	[NS] 44:1;2 (18:1;2-26:0;0)	0.96/0.99
Non-hydroxy-phytosphingosine [NP]	Neg FTMS/MSMS	$[M+C_2H_3O_2+H^-]^-$	$[FA-H^+]^-$	Sub-species	[NP] 46:0;3 (20:0;3-26:0;0)	nd
Non-hydroxy-6-hydroxy-sphingosine [NH]	Neg FTMS/MSMS	$[M+C_2H_3O_2+H^-]^-$	$[FA-H^+]^-$	Sub-species	[NH] 46:1;3 (18:1;3-28:0;0)	nd
Alpha-hydroxy-dehydrosphingosine [ADS]	Neg FTMS/MSMS	$[M+C_2H_3O_2+H^-]^-$	$[FA-H^+]^-$	Sub-species	[ADS] 44:0;3 (19:0;2-25:0;1)	nd
Alpha-hydroxy-sphingosine [AS]	Neg FTMS/MSMS	$[M+C_2H_3O_2+H^-]^-$	$[FA-H^+]^-$	Sub-species	[AS] 44:1;3 (18:1;2-26:0;1)	nd
Alpha-hydroxy-phytosphingosine [AP]	Neg FTMS/MSMS	$[M+C_2H_3O_2+H^-]^-$	$[FA-H^+]^-$	Sub-species	[AP] 42:0;4 (18:0;3-24:0;1)	nd
Alpha-hydroxy-6-hydroxysphingosine [AH]	Neg FTMS/MSMS	$[M+C_2H_3O_2+H^-]^-$	$[FA-H^+]^-$	Sub-species	[AH] 44:1;4 (18:1;3-26:0;1)	nd

Table S1. Lipid classes covered by the method, with mode of their acquisition, ions used for their identification, confirmation and in MSMS-fragmentation scan. FT, fourier transform; M , molecular ion; FA, fatty acid.

Analysis	Subject No.	Age	TEWL ($g/m^2/h$)	Skin conductance (μS)
○	18	63	7.4±0.3	177±5
○	19	69	7.5±0.1	189±14
○	44	48	7.5±0.4	156±21
	38	64	8.3±0.4	94±3
	16	65	9.2±0.1	107±6
	12	63	10.2±0.4	108±4
	31	63	10.4±0.3	249±6
	5	65	10.5±0.3	266±7
	23	28	10.8±0.1	102±5
	36	22	10.8±0.2	68±6
	42	21	11±0.4	51±14
	24	61	11.3±0.3	64±8
	40	21	11.3±0.3	197±25
	6	44	12±0.3	142±13
	10	21	12±0.4	186±11
	22	40	12±0.3	119±13
	41	48	12.2±0.2	84±4
	32	61	12.4±0.3	85±12
	3	47	12.5±0.3	87±7
	4	23	12.7±0.4	37±9
	1	64	13±0.2	75±9
	9	44	13.1±0.3	81±17
	15	64	13.2±0.3	156±15
	21	20	13.4±0.4	198±12
	28	64	13.4±0.4	47±1
	34	20	13.5±0.2	132±18
	29	40	13.8±0.2	167±13
	27	49	14.1±0.4	263±6
	35	47	15.4±0.4	175±12
	2	45	15.5±0.4	229±6
	47	21	15.5±0.3	167±17
○	11	24	15.6±0.5	85±6
	39	20	16.2±0.4	133±14
○	45	25	16.2±0.2	91±8
	13	42	16.7±0.4	176±4
○	37	45	21.6±0.1	48±8

Table S2. Summary of the skin parameters of 36 subjects. TEWL (mean ± S.D.), skin conductance (mean ± S.D.). FPA-based FTIR imaging and quantitative CER analysis were performed on the SC samples of the indicated subjects.

Group	High-TEWL			Low-TEWL		
Subject No.	No. 11	No. 37	No. 45	No. 18	No. 19	No. 44
	56	56	64	81	81	56
	56	56	49	81	81	110
Pixcel count	56	100	81	81	90	64
	100	100	36	90	42	63
	81	42	72	64	64	49
Average	69.8	70.8	60.4	79.4	71.6	68.4
SD	20.1	27.3	18.0	9.5	19.0	24.0

Table S3. Summary of the number of pixels in the analyzed regions. SC cells collected from the high- and low-TEWL subjects were measured by FPA-based FTIR imaging. Each pixel was attributed to a wavenumber derived from the SC cell region. Five SC cell samples were collected independently from each subject.

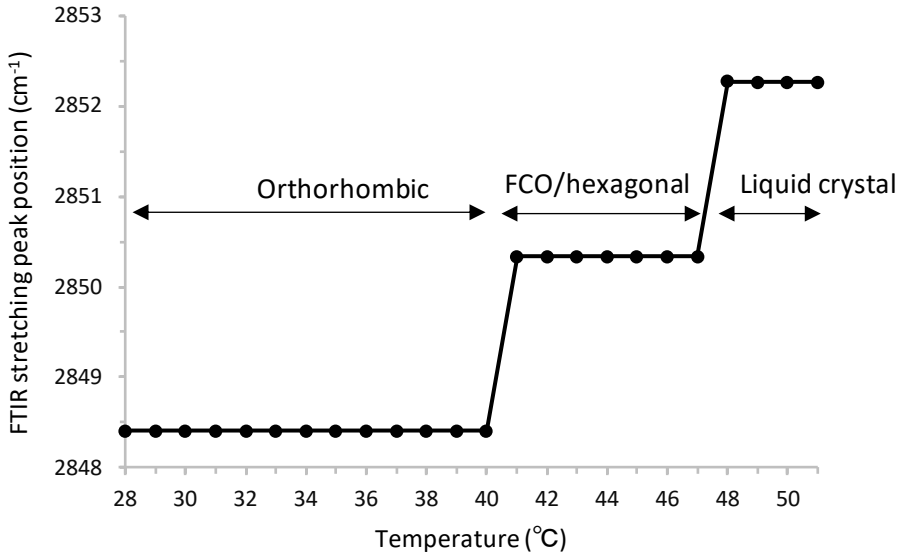

Fig. S2. Temperature dependence of the position of the CH_2 symmetric stretching mode in *n*-tricosane. FCO, face-centered orthorhombic.

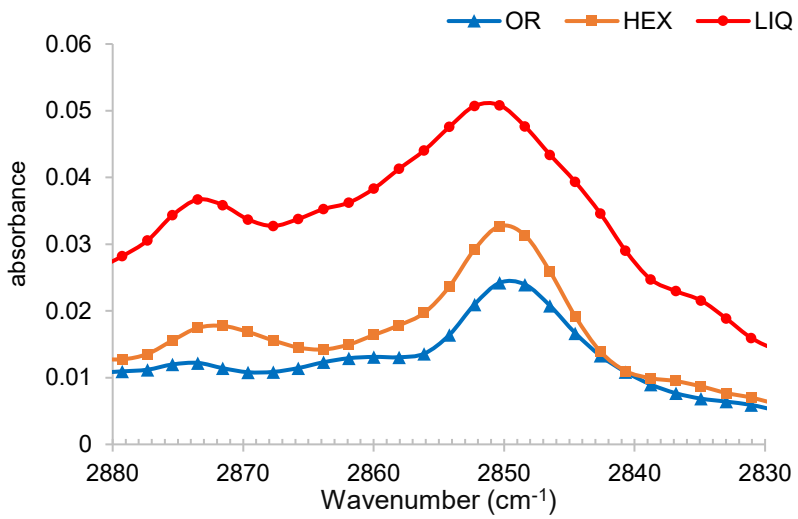

Fig. S3.

Infrared spectral characteristics of the typical CH_2 symmetric stretching vibrations in domains comprising mainly orthorhombic packing (OR), hexagonal packing (HEX), and liquid crystal (LIQ) are shown.

Supplementary Materials and Methods

Intensity counter map of small-angle X-ray scattering of human SC as a function of temperature was also obtained using beamline BL40B2. Measurement conditions were the same as for our intercellular lipid model. The exposure time was 30 s. An approximately 5 mg of the SC was placed in a 1-mm capillary glass tube and placed in the sample holder of the X-ray diffractometer. The temperature of the sample was controlled between 25°C to 85°C using an FP-99 DSC, and the temperature was measured with a thermocouple embedded in the sample holder. All the experiments

were performed with a heating scan at a rate of 0.83 K min^{-1}. The X-ray scattering profile was recorded every 2.5°C.

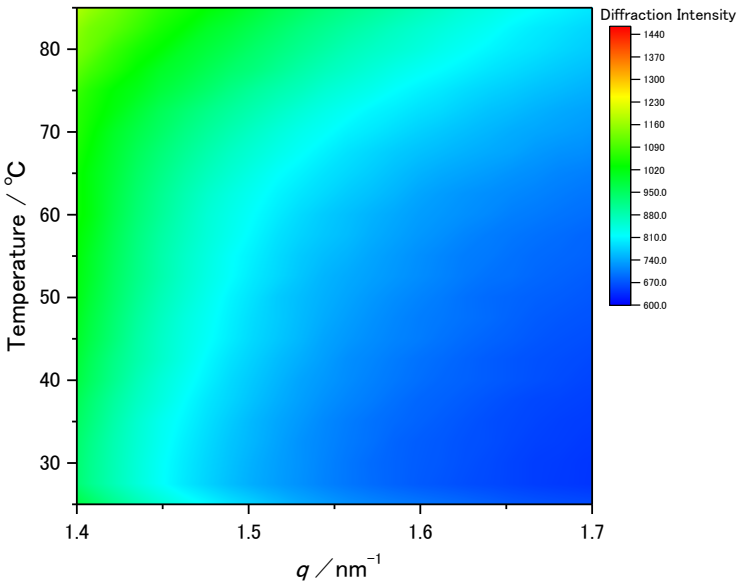

Fig. S4.

Intensity counter map of small-angle X-ray scattering of human SC as a function of temperature (25–85°C). I confirmed the presence of a scattering peak derived from Phase X near $q \approx 1.47$ nm^{-1}.

A noticeable shift in the peak position to the wide-angle side based on the phase transition was observed above 65°C.

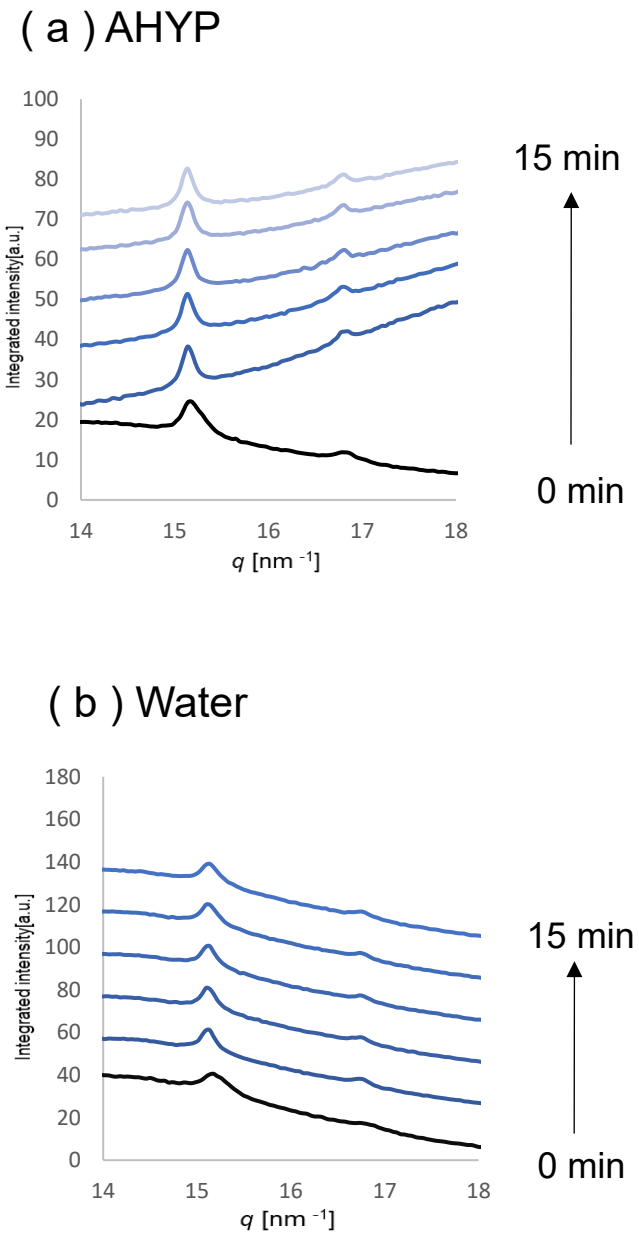

Fig. S5.

WAXD profiles from 0 to 15 min following either AHYP or water application.

WAXD intensity profiles collected from 0 to 15 min following application are indicated by a change in intensity from dark and bright blue (black line: 0 min). WAXD profiles were derived from human SC following the application of either (a) AHYP or (b) water as a control.

Acknowledgements

First of all, I would like to express my gratitude and deepest appreciation to Professor Yasuko Obata for her great advice and guidance in my research and preparing this dissertation.

Secondly, I would like to also express my great appreciation to Dr. Eiji Naru for his helpful guidance and assistance in my research work.

In addition, I wish to thank Dr. Taku Ogura for his valuable suggestions and fruitful discussions.

Moreover, I am grateful to Dr. Noboru Naito, Dr. Akinobu Hayashi, late Mr. Masaki Okuyama, Dr. Keiji Igarashi, Mr. Akihiro Tanaka, Mr. Shinji Kobayashi, Dr. Osamu Sakata, Mr. Masatoshi Sekiya, Dr. Masato Nakade, Dr. Satoshi Onoue, Dr. Ken Inomata, Mr. Kazuyoshi Hamamatsu, Mr. Fumihiko Tsukiyama and all my colleagues of KOSE Corporation for their great assistance and kindness.

Finally, I wish to my sincere gratitude to my wife, son, parents and grandparents. This thesis would not have been fulfilled without their encouragement and support of my study and life.

References

1) Blank I. H., Cutaneous barriers, J. Invest. Dermatol., 45, 249–256 (1965).
2) Barry. B. W., Mode of action of penetration enhancers in human skin, J. Control. Release., 6, 85–97 (1987).
3) Bos J.D., Meinardi M.M., The 500 Dalton rule for the skin penetration of chemical compounds and drugs, Exp. Dermatol., 9, 165–169 (2000).
4) Surber C., Wilhelm K., Maibach H., In vitro and in vivo percutaneous absorption of structurally related phenol and steroid analogs, Eur. J. Pharm. Biopharm., 39, 244–248 (1993).
5) Zhang Q., Grice J. E., Li P., Jepps O. G., Wang G. J., Roberts M. S., Skin solubility determines maximum transepidermal flux for similar size molecules, Pharm. Res., 26, 1974–1985 (2009).
6) Gray G. M., Yardley H. J., Lipid compositions of cells isolated from pig, human, and rat epidermis, J. Lipid Res., 16, 434–440 (1975).
7) Hatta I, Ohta N, Nakazawa H. A possible percutaneous penetration pathway that should be considered. Pharmaceutics., 9, 26, (2017).
8) Bouwstra J. A., Gooris G. S., van der Spek J. A., Bras W., Structural investigations of human stratum corneum by small-angle X-ray scattering, J. Invest. Dermatol., 97, 1005–1012 (1991).
9) Bouwstra J. A., Gooris G. S., Ponec M., The lipid organisation of the skin barrier: liquid and crystalline domains coexist in lamellar phases, J. Biol. Phys., 28, 211–223 (2002).
10) Nakazawa H., Imai T., Hatta I., Sakai S., Inoue S., Kato S., Low-flux electron diffraction study for the intercellular lipid organization on a human corneocyte, Biochim. Biophys. Acta-Biomembr., 1828, 1424–1431 (2013).
11) Janssens M., Van Smeden J., Gooris G. S., Bras W., Portale G., Caspers P. J., Vreeken R. J., Hankemeier T., Kezic S., Wolterbeek R., Lavrijsen A. P., Bouwstra J. A., Increase in short-chain ceramides correlates with an altered lipid organization and decreased barrier function

in atopic eczema patients, J. Lipid Res., 53, 2755–2766 (2012).

12) Damien F., Boncheva M., The extent of orthorhombic lipid phases in the stratum corneum determines the barrier efficiency of human skin in vivo, J. Invest. Dermatol., 130, 611–614 (2010).

13) Janssens M., Mulder A. A., Van Smeden J., Pilgram G. S. K., Wolterbeek R., Lavrijsen A. P. M., Koning R. I., Koster A. J., Bouwstra J. A., Electron diffraction study of lipids in non-lesional stratum corneum of atopic eczema patients, Biochim. Biophys. Acta-Biomembr., 1828, 1814–1821 (2013).

14) Thewalt J., Kitson N., Araujo C., Mackay A., Bloom M., Models of stratum-corneum intercellular membranes: the sphingolipid headgroup is a determinant of phasebehavior in mixed lipid dispersions, Biochem. Biophs. Res. Commun., 188, 1247–1252 (1992).

15) Lafleur M., Phase behaviour of model stratum corneum lipid mixtures: an infrared spectroscopy investigation, Can. J. Chem., 76, 1501–1511 (1998).

16) Moore D. J., Rerek M. E., Insights into the molecular organization of lipids in the skin barrier from infrared spectroscopy studies of stratum corneum lipid models, Acta Derm-Venereol., 16–22 (2000).

17) Watanabe H., Obata Y., Onuki Y., Ishida K., Takayama K., Novel preparation of intercellular lipid models of the stratum corneum containing stereoactive ceramide, Chem. Pharm. Bull., 58, 312–317 (2010).

18) de Jager M., Gooris G., Ponec M., Bouwstra J., Acylceramide head group architecture affects lipid organization in synthetic ceramide mixtures, J. Invest. Dermatol., 123, 911–916 (2004).

19) de Jager M. W., Gooris G. S., Ponec M., Bouwstra J. A., Lipid mixtures prepared with well-defined synthetic ceramides closely mimic the unique stratum corneum lipid phase behavior, J. Lipid Res., 46, 2649–2656 (2005).

20) Janssens M., Gooris G.S., Bouwstra J. A., Infrared spectroscopy studies of mixtures prepared with synthetic ceramides varying in head group architecture: coexistence of liquid and crystalline phases, Biochim. Biophys. Acta-Biomembr., 1788, 732–742 (2009).

21) Wertz P. W., Miethke M. C., Long S. A., Strauss J. S., Downing D. T., The composition of

the ceramides from human stratum-corneum and from comedones, J. Invest. Dermatol., 84, 410–412 (1985).

22) Robson K.J., Stewart M.E., Michelsen S., Lazo N.D., Downing D. T., 6-Hydroxy-4-sphingenine in human epidermal ceramides, J. Lipid Res., 35, 2060–2068 (1994).

23) Stewart M. E., Downing D. T., A new 6-hydroxy-4-sphingenine-containing ceramide in human skin, J. Lipid Res., 40, 1434–1439 (1999).

24) Masukawa Y., Narita H., Shimizu E., Kondo N., Sugai Y., Oba T., Homma R., Ishikawa J., Takagi Y., Kitahara T., Takema Y., Kita K., Characterization of overall ceramide species in human stratum corneum, J. Lipid Res., 49, 1466–1476 (2008).

25) van Smeden J., Hoppel L., van der Heijden R., Hankemeier T., Vreeken R. J., Bouwstra J. A., LC/MS analysis of stratum corneum lipids: ceramide profiling and discovery, J. Lipid Res., 52, 1211–1221 (2011).

26) t'Kindt R., Jorge L., Dumont E., Couturon P., David F., Sandra P., Sandra K., Profiling and characterizing skin ceramides using reversed-phase liquid chromatography–quadrupole time-of-flight mass spectrometry, Anal. Chem., 84, 403–411(2012).

27) Rabionet M., Gorgas K., Sandhoff R., Ceramide synthesis in the epidermis, Biochim. Biophys. Acta-Biomembr., 1841, 422–434 (2014).

28) van Smeden J., Bouwstra J. A., Stratum Corneum lipids: their role for the skin barrier function in healthy subjects and atopic dermatitis patients, Curr. Probl. Dermatol., 49, 8–26 (2016).

29) Sadowski T., Klose C., Gerl M. J., Wójcik-Maciejewicz A., Herzog R., Simons K., Reich A., Surma M. A., Sci. Rep., 7, 43761 (2017).

30) Suzuki M, Ohno Y, Kihara A. Whole picture of human stratum corneum ceramides, including the chain-length diversity of long-chain bases. J Lipid Res., 63,100235 (2022).

31) van Smeden J., Janssens M., Kaye E. C. J., Caspers P. J., Lavrijsen A. P., Vreeken R. J., Bouwstra J. A., The importance of free fatty acid chain length for the skin barrier function in atopic eczema patients, Exp. Dermatol., 23, 45–52 (2014).

32) Bernert Jr. J. T., Sprecher H., An analysis of partial reactions in the overall chain elongation of saturated and unsaturated fatty acids by rat liver microsomes, J.

Biol. Chem., 252, 6736–6744 (1977).

33) A. Jakobsson A., R. Westerberg R., A. Jacobsson A., Fatty acid elongases in mammals: their regulation and roles in metabolism, Prog. Lipid Res., 45, 237–249 (2006)

34) Ohno Y., Suto S., Yamanaka M., Mizutani Y., Mitsutake S., Igarashi Y., Sassa T., Kihara A., ELOVL1 production of C24 acyl-CoAs is linked to C24 sphingolipid synthesis, Proc. Natl. Acad. Sci. U. S. A., 107, 18439–18444 (2010).

35) Kihara A., Very long-chain fatty acids: elongation, physiology and related disorders, J. Biochem., 152, 387–395 (2012).

36) Sassa T., Kihara A., Metabolism of very long-chain fatty acids: genes and pathophysiology, Biomol. Ther. (Seoul), 22, 83–92 (2014).

37) de Jager M., Groenink W., Bielsa i Guivernau R., Andersson E., Angelova N., Ponec M., Bouwstra J., A novel in vitro percutaneous penetration model: evaluation of barrier properties with p-aminobenzoic acid and two of its derivatives, Pharm. Res., 23, 951–960 (2006).

38) Skolova B., Jandovska K., Pullmannova P., Tesar O., Roh J., Hrabalek A., Vavrova K., The role of the trans double bond in skin barrier sphingolipids: permeability and infrared spectroscopic study of model ceramide and dihydroceramide membranes, Langmuir, 30, 5527–5535 (2014).

39) Opalka L., Kovacik A., Maixner J., Vavrova K., Omega-O-Acylceramides in skin lipid membranes: effects of concentration, sphingoid base, and model complexity on microstructure and permeability, Langmuir, 32, 12894–12904 (2016).

40) Skolova B., Kovacik A., Tesar O., Opalka L., Vavrova K., Phytosphingosine, sphingosine and dihydrosphingosine ceramides in model skin lipid membranes: permeability and biophysics, Biochim. Biophys. Acta-Biomembr., 1859, 824–834 (2017).

41) Kováčik A., Pullmannová P., Opálka L., Šilarová M., Maixner J., Vávrová K., Effects of (R)- and (S)-α-hydroxylation of acyl chains in sphingosine, dihydrosphingosine, and phytosphingosine ceramides on phase behavior and permeability of skin lipid models, Int. J. Mol. Sci., 22, 7468 (2021).

42) Uchiyama M., Oguri M., Mojumdar E. H., Gooris G.S., Bouwstra J. A., Free fatty acids

chain length distribution affects the permeability of skin lipid model membranes, Biochim. Biophys. Acta-Biomembr., 1858, 2050–2059 (2016).

43) Uche L. E., Gooris G. S., Bouwstra J. A., Beddoes C. M., Barrier Capability of Skin Lipid Models: Effect of Ceramides and Free Fatty Acid Composition, Langmuir, 35, 15376–15388 (2019).

44) Ramos A. P., Bouwstra J. A., Lafleur M., Very long chain lipids favor the formation of a homogeneous phase in stratum corneum model membranes, Langmuir, 36, 13899–13907 (2020).

45) Uche L.E., Gooris G.S., Bouwstra J.A., Beddoes C.M., Increased Levels of Short-Chain Ceramides Modify the Lipid Organization and Reduce the Lipid Barrier of Skin Model Membranes, Langmuir, 37, 9478–9489 (2021).

46) Motta S, Monti M, Sesana S, Caputo R, Carelli S, Ghidoni R., Ceramide composition of the psoriatic scale., Biochim Biophys Acta., 1182, 147–151 (1993).

47) Loiseau N., Obata Y., Moradian S., Sano H., Yoshino S., Aburai K., Takayama K., Sakamoto K., Holleran W. M., Elias P. M., Uchida Y.. Altered sphingoid base profiles predict compromised membrane structure and permeability in atopic dermatitis, J Dermatol Sci., 72, 296–303 (2013).

48) White S. H., Mirejovsky D., King G. I., Structure of lamellar lipid domains and corneocyte envelopes of murine stratum corneum. An X-ray diffraction study, Biochemistry, 27, 3725–3732 (1988).

49) Mojumdar E. H., Helder R. W., Gooris G. S., Bouwstra J. A., Monounsaturated fatty acids reduce the barrier of stratum corneum lipid membranes by enhancing the formation of a hexagonal lateral packing, Langmuir, 30, 6534–6543 (2014).

50) Doucet J., Potter A., Baltenneck C., Domanov Y. A., Micron-scale assessment of molecular lipid organization in human stratum corneum using microprobe X-ray diffraction, J. Lipid Res.,55, 2380–2388 (2014).

51) Boiten W., Absalah S., Vreeken R., Bouwstra J., van Smeden J., Quantitative analysis of ceramides using a novel lipidomics approach with three dimensional response modelling, Biochim. Biophys. Acta-Mol. Cell Biol. Lipids, 1861, 1652–1661 (2016).

52) Uche L. E., Gooris G. S., Beddoes C. M., Bouwstra J. A., New insight into phase behavior and permeability of skin lipid models based on sphingosine and phytosphingosine ceramides, Biochim. Biophys. Acta-Biomembr., 1861, 1317–1328 (2019).

53) Corbe E., Laugel C., Yagoubi N., Baillet A., Role of ceramide structure and its microenvironment on the conformational order of model stratum corneum lipids mixtures: an approach by FTIR spectroscopy, Chem. Phys. Lipids, 146, 67–75 (2007).

54) Garidel P., Fölting B., Schaller I., Kerth A., The microstructure of the stratum corneum lipid barrier: mid-infrared spectroscopic studies of hydrated ceramide:palmitic acid:cholesterol model systems, Biophys. Chem., 150, 144–156 (2010).

55) Watanabe H., Obata Y., Onuki Y., Ishida K., Takayama K., Different effects of l- and d-menthol on the microstructure of ceramide 5/cholesterol/palmitic acid bilayers, Int. J. Pharm., 402, 146–152 (2010).

56) Engelbrecht T. N., Schroeter A., Hauß T., Bruno D., Scheidt H. A., Huster D., Neubert R. H. H., The impact of ceramides NP and AP on the nanostructure of stratum corneumlipid bilayer. Part I: neutron diffraction and ^{2}H NMR studies on multilamellar models based on ceramides with symmetric alkyl chain length distribution, Soft Matter, 8, 6599–6607 (2012).

57) Schroeter A., Stahlberg S., Školová B., Sonnenberger S., Eichner A., Huster D., Vávrová K., Hauß T., Dobner B., Neubert R. H. H., Vogel A., Phase separation in ceramide[NP] containing lipid model membranes: neutron diffraction and solid-state NMR, Soft Matter, 13, 2107–2119 (2017).

58) Sonnenberger S., Eichner A., Hauß T., Schroeter A., Neubert R. H. H., Dobner B., Synthesis of specifically deuterated ceramide [AP]-C18 and its biophysical characterization using neutron diffraction, Chem. Phys. Lipids, 204, 15–24 (2017).

59) Mueller J., Schroeter A., Steitz R., Trapp M., Neubert R. H. H., Preparation of a New Oligolamellar Stratum Corneum Lipid Model, Langmuir, 32, 4673–4680 (2016).

60) Hatta I., Ohta N., Inoue K., Yagi N., Coexistence of two domains in intercellular lipid matrix of stratum corneum, Biochim. Biophys. Acta-Biomembr., 1758, 1830–1836 (2006).

61) Bangham A. D., Standish M. M., Watkins J. C., Diffusion of univalent ions across the lamellae of swollen phospholipids, J. Mol. Biol., 13, 238–252 (1965).

62) Aburai K., Ogura T., Hyodo R., Sakai H., Abe M., Glatter O., Location of cholesterol in liposomes by using small-angle X-ray scattering (SAXS) data and the generalized indirect Fourier transformation (GIFT) method, J. Oleo Sci., 918, 913–918 (2013).

63) Glatter O., Hainisch B., Improvements in real-space deconvolution of small-angle scattering data, J. Appl. Cryst., 17, 435–441 (1984).

64) Schröter A., Kessner D., Kiselev M. A., Hauß T., Dante S., Neubert R. H. H., Basic nanostructure of stratum corneum lipid matrices based on ceramides [EOS] and [AP]: a neutron diffraction study, Biophys. J., 97, 1104–1114 (2009).

65)Ruettinger A., Kiselev M. A., Hauss T., Dante S., Balagurov A. M., Neubert R. H. H., Fatty acid interdigitation in stratum corneum model membranes: a neutron diffraction study, Eur. Biophys. J., 37, 759–771 (2008).

66) Souza S. L., Capitán M. J., Álvarez J., Funari S. S., Lameiro M. H., Melo E., Phase behavior of aqueous dispersions of mixtures of N-palmitoyl ceramide and cholesterol: a lipid system with ceramide-cholesterol crystalline lamellar phases, J. Phys. Chem. B, 113, 1367–1375 (2009).

67) Bouwstra J. A., Gooris G. S., Dubbelaar F. E. R., Ponec M., Cholesterol sulfate and calcium affect stratum corneum lipid organization over a wide temperature range, J. Lipid Res., 40, 2303–2312 (1999).

68) Petrache H. I., Dodd S. W., Brown M. F., Area per lipid and acyl length distributions in fluid phosphatidylcholines determined by (2)H NMR spectroscopy, Biophys. J., 79, 3172–3192 (2000).

69) Fettiplace R., The influence of the lipid on the water permeability of artificial membranes, Biochim. Biophys. Acta-Biomembr., 513, 1–10 (1978).

70) Uchino T., Hatta I., Miyazaki Y., Onai T., Yamazaki T., Sugiura F., Kagawa Y., Modulation mechanism of the stratum corneum structure during permeation of surfactant-based rigid and elastic vesicles, Int. J. Pharm., 521, 222–231 (2017).

71) Dahle'n B., Pascher I., Molecular arrangements in sphingolipids. Crystal structure of N-tetracosanoylphytosphingosine, Acta Crystallogr. B, 28, 2396–2404 (1972).

72) Dahle'n B., Pascher I., Molecular arrangements in sphingolipids. Thermotropic phase

behaviour of tetracosanoylphytosphingosine, Chem. Phys. Lipids, 24, 119–133 (1979).

73) Raith K., Althoff E., Banse J., Neidhardt H., Neubert R. H. H., Two examples of rapid and simple drug analysis in pharmaceutical formulations using capillary electrophoresis: naphazoline, dexamethasone and benzalkonium in nose drops and nystatin in an oily suspension, Electrophoresis, 19, 2907–2911 (1998).

74) Raudenkolb S., Wartewig S., Neubert R. H. H., Polymorphism of ceramide 3. Part 2: a vibrational spectroscopic and X-ray powder diffraction investigation of N-octadecanoyl phytosphingosine and the analogous specifically deuterated d(35) derivative, Chem. Phys. Lipids, 124, 89–101 (2003).

75) Raudenkolb S., Wartewig S., Neubert R. H. H., Polymorphism of ceramide 6: a vibrational spectroscopic and X-ray powder diffraction investigation of the diastereomers of N-(alpha-hydroxyoctadecanoyl)-phytosphingosine, Chem. Phys. Lipids, 133, 89–102 (2005).

76) Skolova B., Hudska K., Pullmannova P., Kovacik A., Palat K., Roh J., Fleddermann J., Estrela-Lopis I., Vavrova K., Different phase behavior and packing of ceramides with long (C16) and very long (C24) acyls in model membranes: infrared spectroscopy using deuterated lipids, J. Phys. Chem. B, 118, 10460–10470 (2014).

77) Mojumdar E. H., Gooris G. S., Bouwstra J. A., Phase behavior of skin lipid mixtures: the effect of cholesterol on lipid organization, Soft Matter, 11, 4326–4336 (2015).

78) Bouwstra J. A., Gooris G. S., Dubbelaar F. E. R., Ponec M., Phase behavior of lipid mixtures based on human ceramides: coexistence of crystalline and liquid phases, J. Lipid Res., 42, 1759–1770 (2001).

79) Inoue K., Permeability properties of liposomes prepared from dipalmitoyllecithin, dimyristoyllecithin, egg lecithin, rat liver lecithin and beef brain sphingomyelin, Biochim. Biophys. Acta-Biomembr., 339, 390–402 (1974).

80) Seelin A., Seeling J., The dynamic structure of fatty acyl chains in a phospholipid bilayer measured by deuterium magnetic resonance, Biochemistry, 13, 4839–4845 (1974).

81) Uchiyama M., Oguri M., Mojumdar E. H., Gooris G. S., Bouwstra J. A., Free fatty acids chain length distribution affects the permeability of skin lipid model membranes, Biochim. Biophys. Acta-Biomembr., 1858, 2050–2059 (2016).

82) Harding C. R., The stratum corneum: structure and function in health and disease, Dermatol. Ther., 17 (Suppl. 1), 6–15 (2004).

83) Boncheva M., Damien F., Normand V., Molecular organization of the lipid matrix in intact Stratum corneum using ATR-FTIR spectroscopy, Biochim. Biophys. Acta-Biomembr., 1778, 1344–1355 (2008).

84) Nakazawa H., Imai T., Suzuki M., Akakabe N., Hatta I., Kato S., Simultaneous Measurements of Structure and Water Permeability in an Isolated Human Skin Stratum Corneum Sheet, Polymers (Basel), 11, 829 (2019).

85) Berkers T., Visscher D., Gooris G. S., Bouwstra J. A., Topically Applied Ceramides 835, 48 (2018).

86) Leroy M., Lafleur M., Auger M., Laroche G., Pouliot R., Anal., Characterization of the structure of human skin substitutes by infrared microspectroscopy, Bioanal. Chem., 405, 8709–8718 (2013).

87) Brief E., Kwak S., Cheng J. T. J., Kitson N., Thewalt J., Lafleur M., Phase behavior of an equimolar mixture of N-palmitoyl-D-erythro-sphingosine, cholesterol, and palmitic acid, a mixture with optimized hydrophobic matching, Langmuir, 25, 7523–7532 (2009).

88) Oguri M., Gooris G. S., Bito K., Bouwstra J. A., The effect of the chain length distribution of free fatty acids on the mixing properties of stratum corneum model membranes, Biochim. Biophys. Acta-Biomembr., 1838, 1851–1861 (2014).

89) Bhargava R., Wang S., Koenig J. L., FTIR Microspectroscopy of Polymeric Systems, Adv. Polym. Sci., 163, 137–191 (2003).

90) Kawana M., Miyamoto M., Ohno Y., Kihara A., Comparative profiling and comprehensive quantification of stratum corneum ceramides in humans and mice by LC/MS/MS, J. Lipid Res., 61, 884–895 (2020).

91) Joo K. M., Hwang J. H., Bae S. J., Nahm D. H., Park H. S., Ye Y. M., Lim K. M., Relationship of ceramide-, and free fatty acid-cholesterol ratios in the stratum corneum with skin barrier function of normal, atopic dermatitis lesional and non-lesional skins, J. Dermatol. Sci., 77, 71–74 (2015).

92) Laffet G. P., Genette A., Gamboa B., Auroy V., Voegel J. J., Determination of fatty acid and

sphingoid base composition of eleven ceramide subclasses in stratum corneum by UHPLC/scheduled-MRM, Metabolomics, 14, 69 (2018).

93) Boiten W. A., Berkers T., Absalah S., van Smeden J., Lavrijsen A. P. M., Bouwstra J. A., Applying a vernix caseosa based formulation accelerates skin barrier repair by modulating lipid biosynthesis, J. Lipid Res., 59, 250–260 (2018).

94) Small D. M., Lateral chain packing in lipids and membranes, J. Lipid Res., 25, 1490–1500 (1984).

95) Ungar G., Mašić N., Order in the rotator phase of n-alkanes, J. Phys. Chem., 89, 1036–1042 (1985).

96) Nouar H., Petitjean D., Bouroukba M., Dirand M., Binary phase diagram of the system: n-docosane-n-tricosane, J. Mol. Struct., 443, 197–204 (1998).

97)) Shin J. H., Shon J. C., Lee K., Kim S., Park C. S., Choi E. H., Lee C. H., Lee H. S., Liu K. H., A lipidomic platform establishment for structural identification of skin ceramides with non-hydroxyacyl chains, Anal. Bioanal. Chem., 406, 1917–1932 (2014).

98) Wu Z., Shon J. C., Lee D., Park K. T., Park C. S., Lee T., Lee H. S., Liu K. H., Lipidomic platform for structural identification of skin ceramides with α-hydroxyacyl chains, Anal. Bioanal. Chem., 408, 2069–2082 (2016).

99) Surma M. A., Herzog R., Vasilj A., Klose C., Christinat N., Morin-Rivron D., Simons K., Masoodi M., Sampaio J. L., An automated shotgun lipidomics platform for high throughput, comprehensive, and quantitative analysis of blood plasma intact lipids, Eur. J. Lipid Sci. Technol., 117, 1540–1549 (2015).

100) Masukawa Y., Narita H., Sato H., Naoe A., Kondo N., Sugai Y., Oba T., Homma R., Ishikawa J., Takagi Y., Kitahara T., Comprehensive quantification of ceramide species in human stratum corneum, J. Lipid Res., 50, 1708–1719 (2009).

101) Voegeli R., Heiland J., Doppler S., Rawlings A. V., Schreier T., Efficient and simple quantification of stratum corneum proteins on tape strippings by infrared densitometry, Skin Res. Technol., 13, 242–251 (2007).

102) Hatta I., Nakazawa H., Obata Y., Ohta N., Inoue K., Yagi N., Novel method to observe subtle structural modulation of stratum corneum on applying chemical agents, Chem. Phys.

Lipids, 163, 381–389 (2010).

103) Ohnari H., Naru E., Ogura T., Sakata O., Obata Y., Phase Separation in Lipid Lamellae Result from Ceramide Conformations and Lateral Packing Structure, Chem. Pharm. Bull., 69, 72–80 (2021).

104) Ohnari H., Sekiya M., Naru E., Ogura T., Sakata O., Obata Y., Amino acids and their n-acetylated derivatives maintain the skin's barrier function, Chem. Pharm. Bull., 69, 652–660 (2021).

105) Egawa M., Yanai M., Maruyama N., Fukaya Y., Hirao T., Visualization of water distribution in the facial epidermal layers of skin using high-sensitivity near-infrared (NIR) imaging, Appl. Spectrosc., 69, 481–487 (2015).

106) Voegeli R., Rawlings A. V., Seroul P., Summers B., Int. A novel continuous colour mapping approach for visualization of facial skin hydration and transepidermal water loss for four ethnic groups, J. Cosmet. Sci., 37, 595–605 (2015).

107) Pilgram G. S. K., Engelsma-Van Pelt A. M., Bouwstra J. A., Koerten H. K., Electron diffraction provides new information on human stratum corneum lipid organization studied in relation to depth and temperature, J. Invest. Dermatol., 113, 403–409 (1999).

108) Nakazawa H., Ohta N., Hatta I., A possible regulation mechanism of water content in human stratum corneum via intercellular lipid matrix, Chem. Phys. Lipids, 165, 238–243 (2012).

109) Wang X., Ujihara M., Imae T., Saiwaki T., Ishikubo A., Okamoto T., Visual observation of selective elution of components from skin-mimetic lipid membrane, Colloids Surf. B Biointerfaces, 81, 174–177 (2010).

110) Yoshida S., Obata Y., Onuki Y., Utsumi S., Ohta N., Takahashi H., Takayama K., Molecular Interaction between Intercellular Lipids in the Stratum Corneum and l-Menthol, as Analyzed by Synchrotron X-Ray Diffraction, Chem. Pharm. Bull., 65, 134–142 (2017).

111) Utsumi S., Nakamura T., Obata Y., Ohta N., Takayama K., Effect of Nerolidol and/or Leulinic Acid on the Thermotropic Behavior of Lipid Lamellar Structures in the Stratum Corneum, Chem. Pharm. Bull., 64, 1692–1697 (2016).

112) Obata Y., Hatta I., Ohta N., Kunizawa N., Yagi N., Takayama K., Combined effects of

ethanol and L-menthol on hairless rat stratum corneum investigated by synchrotron X-ray diffraction, J. Control. Release, 115, 275–279 (2006).

113) Horita D., Hatta I., Yoshimoto M., Kitao Y., Todo H., Sugibayashi K., Molecular mechanisms of action of different concentrations of ethanol in water on ordered structures of intercellular lipids and soft keratin in the stratum corneum, Biochim. Biophys. Acta-Biomembr., 1848, 1196–1202 (2015).

114) Berkers T., van Dijk L., Absalah S., van Smeden J., Bouwstra J. A., Topically applied fatty acids are elongated before incorporation in the stratum corneum lipid matrix in compromised skin, Exp. Dermol., 26, 36–43 (2017).

115) Nakaune-Iijima A., Sugishima A., Omura G., Kitaoka H., Tashiro T., Kageyama S., Hatta I., Topical treatments with acylceramide dispersions restored stratum corneum lipid lamellar structures in a reconstructed human epidermis model, Chem. Phys. Lipids, 215, 56–62 (2018).

116) Gooris G. S., Kamran M., Kros A., Moore D. J., Bouwstra J. A., Interactions of dipalmitoylphosphatidylcholine with ceramide-based mixtures, Biochim. Biophys. Acta-Biomembr., 1860, 1272–1281 (2018).

117) Rawlings A. V., Harding C. R., Moisturization and skin barrier function, Dermatol. Ther., 17 (Suppl. 1), 43–48 (2004).

118) Pashkovskaya A. A., Vazdar M., Zimmermann L., Jovanovic O., Pohl P., Pohl E. E., Mechanism of long-chain free fatty acid protonation at the membrane-water interface, Biophys. J., 114, 2142–2151 (2018).

119) Hashizume E., Nakano T., Kamimura A., Morishita K., Topical effects of N-acetyl-L-hydroxyproline on ceramide synthesis and alleviation of pruritus, Clin. Cosmet. Investig. Dermatol., 6, 43–49 (2013).

120) Garson J. C., Doucet J., Lévêque J. L., Tsoucaris G., Oriented structure in human stratum corneum revealed by X-ray diffraction, J. Invest. Dermatol., 96, 43–49 (1991).

121) Moore D. J., Rerek M. E., Mendelsohn R., Lipid domains and orthorhombic phases in model stratum corneum: evidence from Fourier transform infrared spectroscopy studies, Biochem. Biophys. Res. Commun., 231, 797–801 (1997).

122) Lieckfeldt R., Villalaín J., Gómez-Fernández J. C., Lee G., Apparent pKa of the fatty acids within ordered mixtures of model human stratum corneum lipids, Pharm. Res., 12, 1614–1617 (1995).

123) Mark H., Harding C. R., Amino acid composition, including key derivatives of eccrine sweat: potential biomarkers of certain atopic skin conditions, Int. J. Cosmet. Sci., 35, 163–168 (2013).

124) Visscher M. O., Tolia G. T., Wickett R. R., Hoath S. B., Effect of soaking and natural moisturizing factor on stratum corneum water-handling properties, J. Cosmet. Sci., 54, 289–300 (2003).

125) Arseneault M., Lafleur M., Biophys. J., 92, 99–114 (2007).

126) Iwai I., Kunizawa N., Yagi E., Hirao T., Hatta I., Stratum corneum drying drives vertical compression and lipid organization and improves barrier function in vitro, Acta Derm. Venereol., 93, 138–143 (2013).

127) Hills A. G., pH and the Henderson-Hasselbalch equation, Am. J. Med., 55, 131–133 (1973).

128) Narangifard A., Wennberg C. L., Lianne den Hollander L. D., Iwai I., Han H., Lundborg M., Masich S., Lindahl E., Daneholt B., Norlén L., Molecular Reorganization during the Formation of the Human Skin Barrier Studied In Situ, J. Invest. Dermatol., 141, 1243–1253 (2020).

129) Chen X., Kwak S., Lafleur M., Bloom M., Kitson N., Thewalt J., Fatty acids influence "solid" phase formation in models of stratum corneum intercellular membranes, Langmuir, 23, 5548–5556 (2007).